Nanoscale

In situ transmission electron microscopy insights into nanoscale deformation mechanisms of body-centered cubic metals

Journal:	*Nanoscale*
Manuscript ID	NR-REV-09-2024-004007.R1
Article Type:	Review Article
Date Submitted by the Author:	07-Nov-2024
Complete List of Authors:	Li, Hai; Southeast University Sheng, Ming; Southeast University Luo, Kailin; Southeast University Liu, Min; Southeast University Tan, Qiuyang; Southeast University Chen, Sijing; Southeast University Zhong, Li ; Southeast University Sun, Litao; Southeast University, Key Laboratory of MEMS of Ministry of Education

In situ transmission electron microscopy insights into nanoscale deformation mechanisms of body-centered cubic metals

Hai Li, Ming Sheng, Kailin Luo, Min Liu, Qiuyang Tan, Sijing Chen*, Li Zhong*, Litao Sun

SEU-FEI Nano-Pico Center, Key Laboratory of MEMS of Ministry of Education, School of Integrated Circuits, Southeast University, Nanjing 210096, China;

* Correspondence to: 101300228@seu.edu.cn, lizhong@seu.edu.cn

Abstract: Nanostructured body-centered cubic (BCC) metals exhibit remarkable mechanical properties under various stress fields, making them promising candidates for novel micro/nanoelectromechanical systems (M/NEMS). A deep understanding of their mechanical behaviors, particularly at the atomic scale, is essential for optimizing their properties and expanding their applications at the nanoscale. Newly developed nanomechanical testing techniques inside the transmission electron microscopes (TEM) provide powerful tools for uncovering the atomic-scale microstructural evolution of nanostructured BCC materials under external forces. This article reviews recent progresses in the experimental methods used in the in situ TEM nanomechanical testing, and the achievements of these techniques in understanding the deformation mechanisms of BCC nanomaterials. By outlining the current challenges and future research directions, this review aims to inspire continued exploration in the nanomechanics of BCC metals, contributing to the development of advanced BCC nanomaterials with tailored mechanical properties.

Keywords: nanostructured BCC materials; nanomechanics; in situ TEM; deformation mechanisms

1. Introduction

BCC metals are of great significance in engineering materials and high-temperature applications, due to their exceptional strength and thermal stability[1-5]. Given the phenomenon of "smaller is stronger", nanosized BCC metals are anticipated to outperform their bulk counterparts in mechanical properties[6, 7]. It has been identified that nanosized BCC metals have shown excellent performance in micro/nanoelectromechanical devices and integrated circuits (ICs)[8-13]. For example, nanocrystalline tantalum (Ta) has been successfully integrated into MEMS thermal actuators, where it demonstrates exceptional performance for mechanical property measurements[11, 14, 15]. Additionally, molybdenum (Mo) is being explored as a promising alternative to copper (Cu) for metal interconnect materials[12, 13]. However, as the dimensions of BCC metals decrease, surface and size effects become increasingly pronounced, leading to deformation mechanisms distinct from those observed in bulk BCC metals. Specifically, plastic deformation in bulk BCC metals is predominantly governed by the motion of screw dislocations[16, 17]. In contrast, nanosized BCC metals exhibit additional deformation mechanisms, such as twinning and phase transformation[18, 19]. Gaining a deeper understanding of the mechanical behavior of BCC nanostructured materials, especially at the atomic level, is essential for

enhancing their properties and expanding their applications in nanomaterials and devices. However, in BCC metals, such as vanadium (V), α-iron (α-Fe), niobium (Nb), Mo, Ta, and tungsten (W), the intrinsic high lattice resistance[16, 20] and non-planar core structure of 1/2<111> screw dislocations give rise to strong temperature and strain rate sensitivity of the yield strength[21-26]. Furthermore, the outstanding features of the slip geometry may spread into several planes of the <111> zone[27]. These factors make experimental characterization of BCC metals extremely challenging. The unique deformation characteristics of BCC metals, including a limited number of slip systems, low-temperature brittleness, pronounced strain hardening, and a tendency for cross-slip[23, 28, 29], further complicate experimental analysis. Molecular dynamics (MD) simulations dominated the mechanistic insights into atomic-scale deformation behaviors of BCC nanomaterials for a long time[21, 30-38]. Although informative, MD simulations face several limitations, including the use of excessively high strain rates[39], lack of accurate inter-atomic potentials[40], and the inability to fully represent veritable crystal structures[41]. To solve these inadequacies, there is an urgent need to acquire real-time atomic-scale experiments to validate the discoveries, thereby posing a higher challenge to the development of nanotechnology.

In the recent decade, facilitated by the development of TEM imaging techniques and nanofabrication technologies, in situ TEM[18, 42-50] has

become capable of simultaneous real-time atomic-scale imaging and quantitative mechanical testing[51-54]. In situ TEM provides an intuitive dynamic process of deformation and it is also possible to tune the microstructure by using electrical[55], thermal[56], and stress fields[57], improving the understanding of the deformation mechanisms. It has been found that dislocation, twinning, and phase transformation are key deformation mechanisms in metallic materials. While there is competition between various deformation modes, such as between dislocation motion and twinning at different scales[58, 59], these mechanisms are also closely interconnected. For example, both phase transformation and twinning are fundamentally influenced by dislocation activity[60-63]. Additionally, phase transformation can facilitate twinning deformation[64, 65], and dislocations can transform into twins[59, 66, 67], etc. However, some mechanisms have not yet been discovered by experiments, such as whether twin or phase transformation can be transformed to dislocation. Thus, it is necessary to understand these deformation modes in depth, and reveal the correlations at atomic scale. This article provides a comprehensive review of the mechanical testing of BCC metals using in situ TEM, highlighting the available experimental techniques and summarizing recent progress in understanding the deformation mechanisms of nanosized BCC metals, including dislocation behavior, twinning deformation, and phase transformation (Fig. 1). In addition, future research directions and the

challenge of in situ TEM studies on nanostructured materials are discussed.

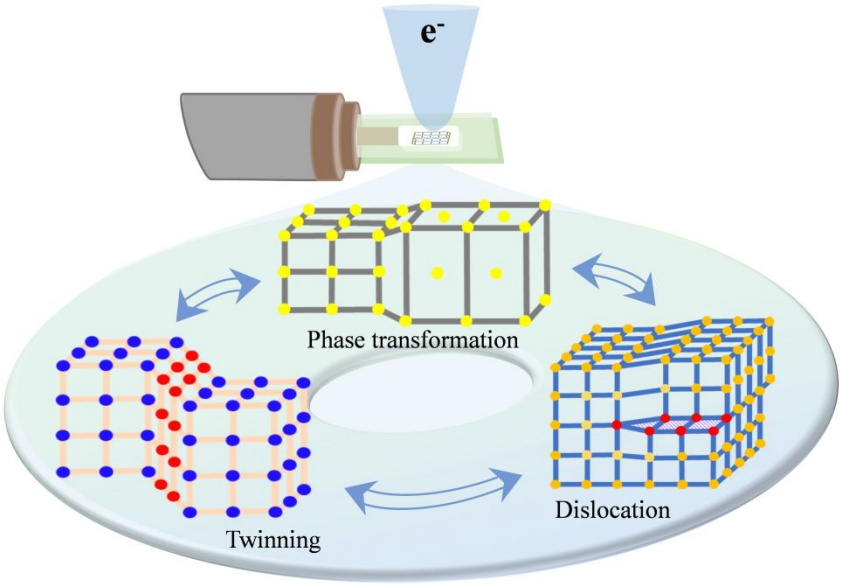

Fig. 1 Schematic summary of deformation mechanisms and their interrelationships in BCC metals by situ TEM.

2. In situ TEM nanomechanical testing techniques

In situ TEM nanomechanical testing involves utilizing functional holders to perform loading on nanoscale samples while employing TEM to observe their behave under loading in real-time. TEM holders provide stable platforms for sample loading or other operations. Nowadays, various types of holders have been designed for mechanical testing, ranging from simple motorized holder to those equipped with elaborate grips. The advanced equipment and technique offer unprecedented insights into the behavior of materials at nanoscale, which is critical for

improving their mechanical performances. Here are the most commonly used techniques:

2.1 Classical tensile technique

The classic tension holder primarily consists of a straining substrate prepared from a commercially available copper (Cu) film. Samples are attached to the substrate and then fixed to a pair of pins (Fig. 2a). The loading is controlled by an electric motor outside the TEM instrument[68]. This technique has a wide range of applicability, allowing the study of various thin or thinned samples[69-71]. In addition to in situ straining at room temperature, heating or cooling equipment can be incorporated during loading[44]. Despite the extreme versatility of this technique, it is exemplified by observations of dislocation motion[72] and grain boundary (GB) activities[73, 74] that the precision of motor movements is comparatively insufficient to realize atomic-scale observations of the microstructural evolution. The classic tension holder commonly uses twin-jet electropolishing as a sample preparation method. In sample preparation, selecting an appropriate twin-jet electrolyte and maintaining an optimal preparation temperature, as well as determining the stress area for TEM observation are crucial.

2.2 Nanoindentation technique

The in situ TEM nanoindentation technique was first proposed in 1995 and initially applied to investigate the deformation behavior of

silicon (Si) single crystal in 1998[75]. Nanoindentation is a technique used to measure the mechanical properties of materials on a micro/nanometer scale. The basic principle involves pressing an indenter, typically made of diamond, into the surface of a material while recording the applied force and the corresponding indentation depth. By analyzing the load-displacement data, key mechanical properties such as hardness, elastic modulus, and plastic deformation can be determined[76-78]. Nanoindenters are often equipped with load sensors that can complement real-time load-displacement curves for structural evolution[45], providing more quantitative data for in situ experiments and analysis. Nowadays, commercial nanoindenters are widely used to deform metals and plasticity mechanisms[53, 79, 80] (Fig. 2b). Taking advantage of the development in sample preparation via focused ion beam (FIB), more flexible designs of samples have been successfully incorporated into the in situ nanoindentation experiments, such as nanopillars[81], wedges[82], or H-bars[83] (Fig. 2c). However, FIB milling has limitations in sample preparation, as it can introduce defects like vacancies, interstitials, or dislocations, potentially impacting experimental results. Annealing can help minimize these effects[84]. In addition to the diverse sample designs, the shape of the nanoindenter can also be customized to cater to different loading modes, such as tensile loading[85] (Fig. 2d).

2.3 MEMS-based techniques

MEMS-based platforms are widely used in nanomechanical testing[86, 87], owing to their capabilities of precise control actuation, independent load sensing and measurement, while simultaneously allowing observation at atomic-scale[88, 89]. Zhu and Espinosa[90] were among the first to develop a MEMS platform for in situ nanomechanical testing, which is integrated with the Si platform that is elastically deformable in strain and a pair of facing pads to attach samples[91] (Fig. 2e). The use of advanced nanofabrication techniques allows the creation of diverse geometries[89, 91, 92] for mechanical testing with high accuracy, which is beneficial for nanostructure samples with different scales, especially for creating tests with boundary conditions. However, observing structural evolution at the atomic scale at high temperature remains challenging. Recently, Han et al.[93] developed a novel MEMS-based high-temperature mechanical testing stage (Fig. 2f), which allows mechanical testing under temperature approaching 1560 K and atomic-scale observation. Such multi-field coupling platform based on MEMS offers opportunities for a more comprehensive understanding of mechanical properties. However, most of these MEMS platforms are highly dependent on fairly complex setups, making their implementation and operation both challenging and costly. Therefore, avoiding damage to the MEMS structure during transfer and processing is essential.

2.4 Sequential fabrication-testing technique

The sequential fabrication-testing technique is based on scanning tunneling microscopy (STM)-TEM holder (Fig. 2g), where the probe can be driven by electrostatic deflection or mechanical resonance, enabling the realization of deformation (tension, compression, bending, or shear) by effectively manipulating the nanostructures with different sizes[42, 51, 94-96], and geometries[18, 57, 97] with the atomic resolution. Specifically, the probe with a piezo-controller as one side of the stage, a bulk metal rod with nanoscale surface edges[18], semi-copper mesh[98], a gold wire with nanoscale samples[99], a sample fabricated by FIB[100], or atomic force microscopy (AFM) cantilever[51] as the other side of the TEM stage (Fig. 2h). By connecting the sample and probe through the controller via electric pulse welding[101] or potential-introduced welding[18], various nanostructures can be fabricated, including single[42], bi-crystal[96], and nanotwinned samples[102] with different sizes and orientations[18]. This technique makes it feasible to study the effects of various material and geometrical factors on the deformation of nanostructured materials. In addition to the limitation that the crystal orientation can only be adjusted in one dimension, the challenges of this technique lie in the pre-preparation of the sample and the process parameters, for example, modulation of current voltage for the preparation of single or bi-crystal nanowires.

2.5 Thermal-bimetallic-based technique

Han et al.[103] developed a novel in situ strain device for TEM (Fig. 2i), which can slowly and gently deform single or polycrystalline materials while retaining the double-tilt capability for performing in situ atomic-scale observations[104-107]. This method can even measure regular samples, including thin-films[19, 106, 108-110], nanowires[43, 111, 112], and nanoflake[113-116], assisted by FIB fabrication. The key to this device is bimetallic strips with different thermal expansion coefficients[108, 117]. The two plates are fixed on a TEM Cu-ring grid, which can be arranged to bend slowly in opposite directions. As the bimetallic are fixed on the Cu-ring grid with superglue, the operation temperature is usually below ~ 200 ℃ to avoid superglue evaporation[48].

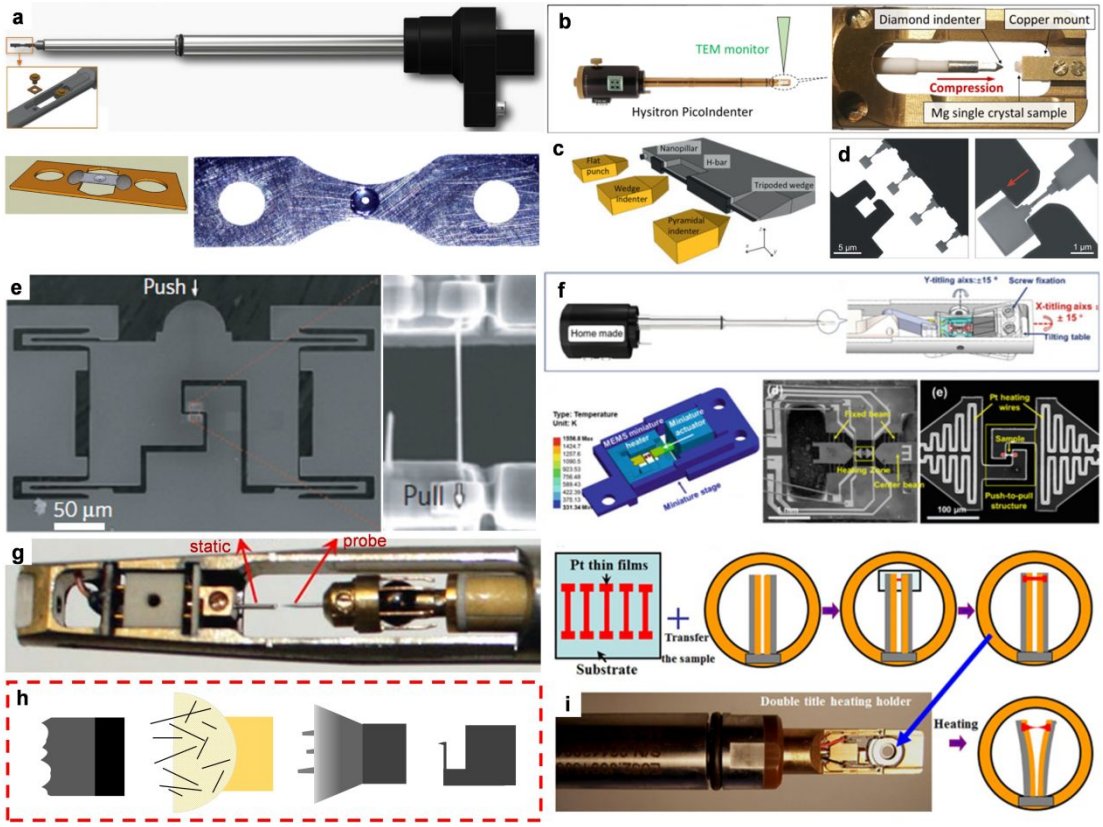

Fig. 2 (a) The picture of Gatan model 654 single-tilt straining holder and

the Cu plate. Reproduced with permission from ref. [46], Copyright 2014, Elsevier Masson. (b) A Hysitron PicoIndenter (PI95) holder, the pillar was compressed by a diamond indenter with a flat punch by the inset. Reproduced with permission from ref. [53], Copyright 2019, American Association for the Advancement of Science. (c) Sketch of the various types of straining configurations used in the nanoindentation holders, Reproduced with permission from ref. [46], Copyright 2014, Elsevier Masson. (d) The microfabricated bridge samples and corresponding tensile gripper. Reproduced with permission from ref. [85], Copyright 2021, American Association for the Advancement of Science. (e) A typical MEMS tension device and a secured nanowire. Reproduced with permission from ref. [87], Copyright 2015, Springer Nature. (f) The custom-designed in situ thermomechanical TEM sample holder, Reproduced with permission from ref. [93], Copyright 2021, Springer Nature. (g) A TEM-STM holder. (h) The illustrations are different types of samples. (i) A Gatan double-tilt heating holder with two thermal bimetallic strips tension device installed. Reproduced with permission from ref. [107], Copyright 2018, Chinese Society of Metals.

The above are the commonly used in situ TEM mechanical testing techniques, which can be selected for different materials and experimental purposes. Table 1 provides an intuitive comparison of these

in situ TEM techniques.

Table 1 Comparison between different techniques

	Loading conditions	Common loading rate	Temperature range	Spatial resolution	Sample size	Sample type	FIB assist	Quantification
Classical tensile technique[118]	tensile	0.01~ 1 μm/s	RT, heating or cooling	nano-scale	sub-micron	thin film nanowire nanoplate	depends on the sample	no
Nanoindentation technique[119]	tensile compress indentation	1 ~ 10 nm/s	RT	nano-scale	sub-micron	sub-micron pillar nanoplate	yes	yes
MEMS-based techniques[93]	tensile compress	10^{-4}~10^{-2} nm/s	RT-1200 ℃	atomic-scale	nano-scale, sub-micron	nanowire nanoplate	yes	yes
Sequential fabrication-testing technique[66]	tensile compress bending or shear	10^{-4}~10^{-2} nm/s	RT	atomic-scale	nano-scale, sub-micron	nanowire nanopillar nanoplate	depends on the sample	no AFM/yes
Thermal-bimetallic-based technique[106]	tensile	10^{-4}~10^{-3} nm/s	< 80 ℃	atomic-scale	nano-scale, sub-micron	thin film nanowire nanoplate	depends on the sample	no

3. Dislocation behaviors in BCC nanocrystals

Dislocation plays a crucial role in the plastic deformation of BCC materials[120-122], which effect plasticity in many aspects, including mechanical responses[16, 123], plastic morphology[124, 125], and plastic deformation mechanisms[18]. Since the mechanical behaviors at small scales exhibits size-dependent deviations from the classic theories[126], it is critical to explore the underlying deformation mechanisms to fully understand the mechanical properties at small scales. Nonetheless, the dynamic processes of deformation and failure of nanosized BCC metals remain poorly understood. In situ TEM mechanical testing provides an opportunity to directly capture the dynamic dislocation behaviors in the small-sized samples and thus uncover new deformation mechanisms or

behaviors that are fundamentally different from bulk metals.

3.1 Dislocation starvation in BCC nanocrystals

Theoretical and experimental studies have indicated that mechanical size effects are related to dislocation mechanisms and the consequence of increased surface-to-volume ratios at the nanoscale[24, 127]. The large surface-to-volume ratio can facilitate dislocation escape from the free surface before entanglement. It has been shown that in small volume face-centered cubic (FCC) metals, mobile dislocations can easily escape from the free surface, leading to source exhaustion and dislocation starvation[128-132]. Although exhaustion and starvation have been suggested to exist in BCC metals[124, 133], they have not yet been observed. When the diameters decrease to hundreds of nanometers, significant mechanical annealing occurs in BCC materials[134]. Minor et al.[119] used in situ TEM nanoindentation to investigate that Mo-alloy nanofibers with preexisting defects could be mechanically annealed to a dislocation-free state under tensile loading. By correlating the TEM and stress-strain data, it can be seen that the first dislocation escaped from the fiber under tension loading (Fig. 3a), corresponding to a stress of 297 MPa (Fig. 3b), while the remaining dislocations annihilated at subsequent loading. This result shows that dislocation starvation occurs in the BCC materials. In addition, the same behavior has also been observed in compression of α-Fe (Fig. 3c, d), Mo and V nanopillars[134-136]. As the dislocation starvation

increases and dislocation sources are exhausted, the flow stress of the sample increases, leading to hardening. Once dislocation starvation is complete, the samples yielded catastrophically[119, 127]. However, some findings suggest that, in BCC pillars, dislocations undergo self-multiplication rather than annihilation[127, 137]. This is a significant difference between the dislocation behaviors of BCC and FCC metals. In FCC metals, dislocations typically nucleate and then escape the pillar. In contrast, BCC metals can generate multiple new dislocations[138]. Ryu et al.[139] pointed out that there is a competition between dislocation multiplication and depletion in micropillars, which is related to the strain rates. Monavari et al.[140] showed that both processes are associated with changes in the volume density of dislocation loops: dislocation annihilation needs to be envisaged in terms of the merging of dislocation loops, while conversely dislocation multiplication is associated with the generation of new loops. These understandings, however, are based on simulations and need further experimental confirmation.

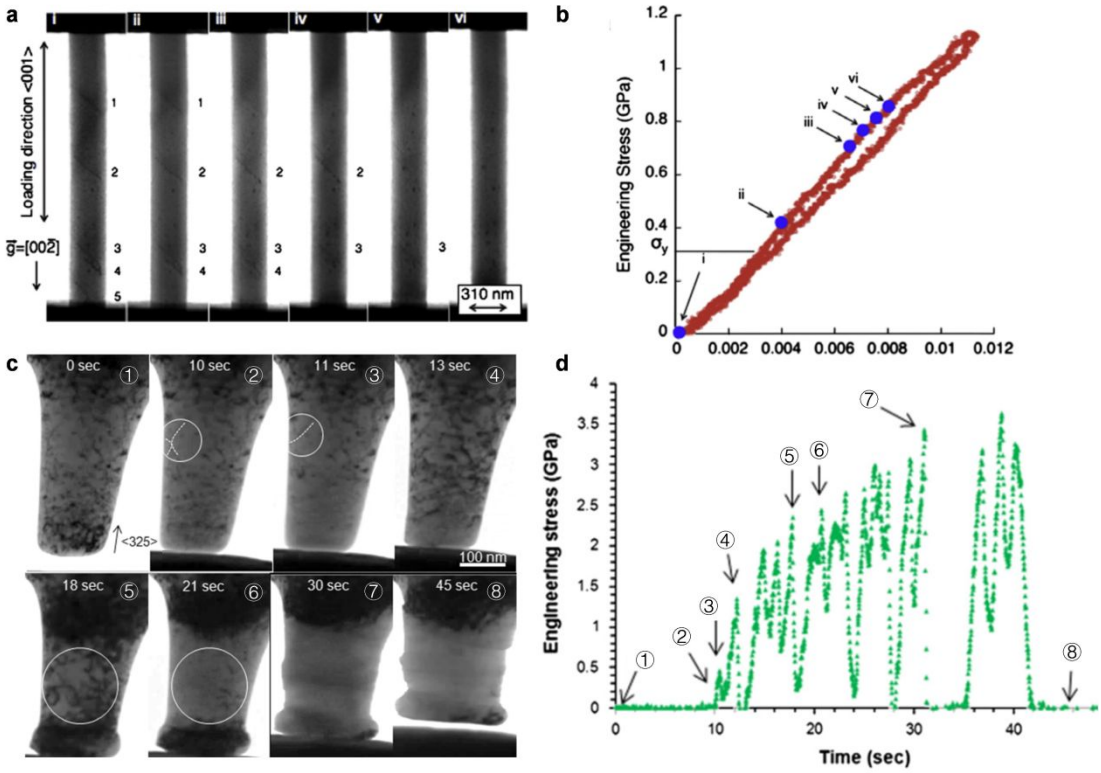

Fig. 3 Mechanical annealing behavior in BCC metals. (a) Time series of a Mo-alloy fiber tilted to the [100] zone axis and loaded at a displacement rate of 2 nm/s under <001> direction, the dislocations escape from the fiber. (b) Engineering stress-strain curve of an intermediate dislocation density fiber that displays both exhaustion hardening and dislocation starvation. Reproduced with permission from ref. [119], Copyright 2012, Elsevier Ltd. (c) Still bright-field TEM images showing the deformation behavior from the in situ nanocompression test on a high dislocation density with clusters pillar 150 nm in diameter at a rate of 5 nm/s along the [325] direction displaying the process of mechanical annealing. (d) Measured stress-time data; the individual still images are indicated. Reproduced with permission from ref. [134], Copyright 2013, Elsevier

Ltd.

3.2 Surface-mediated dislocation nucleation

With further reduction of crystal size, the free surface becomes an effective nucleation site for dislocations in BCC metals[18, 113, 127, 141]. Wang et al.[18] prepared high quality nanowires using sequential fabrication-testing technique and reported that 1/2<111> -type mixed dislocations nucleate simultaneously from multiple surface sites with the estimated shear stress about 7.2 GPa on the (101) slip planes when the BCC W nanowires are loaded along the <112> direction (Fig. 4a). They pointed out that most of these dislocations seem to as dipoles (Fig. 4c), which are probably the half dislocation loops on (101) planes. Dislocations in dipoles can expand on their slip planes under further loading (Fig. 4d), contributing to plastic deformation (Fig. 4e, f). Under high strain, the multiple dislocation nucleation sites changed from the (101) plane to the (111) plane[141], forming a preferential dislocation nucleation region and leading to discrete thickening of the shear band (Fig. 4g-j). The interface-dominated deformation and thickening mechanism of the shear band may have been applied to understand the deformation of the other nanosized structures. In addition, in nanowires of relatively large samples (~45 nm), Wang et al.[142] directly observed a half-dislocation loop with the Burgers vector of 1/2<111>{110} was nucleated from the free surface and then

expanded into the nanowire. The surface intersection point of the expanding dislocation loop could act as an effective pinning point for dragging dislocation motion, causing slow rotation of the dislocation line around the pinning point and escape from the surface under further straining (Fig. 4k-o).

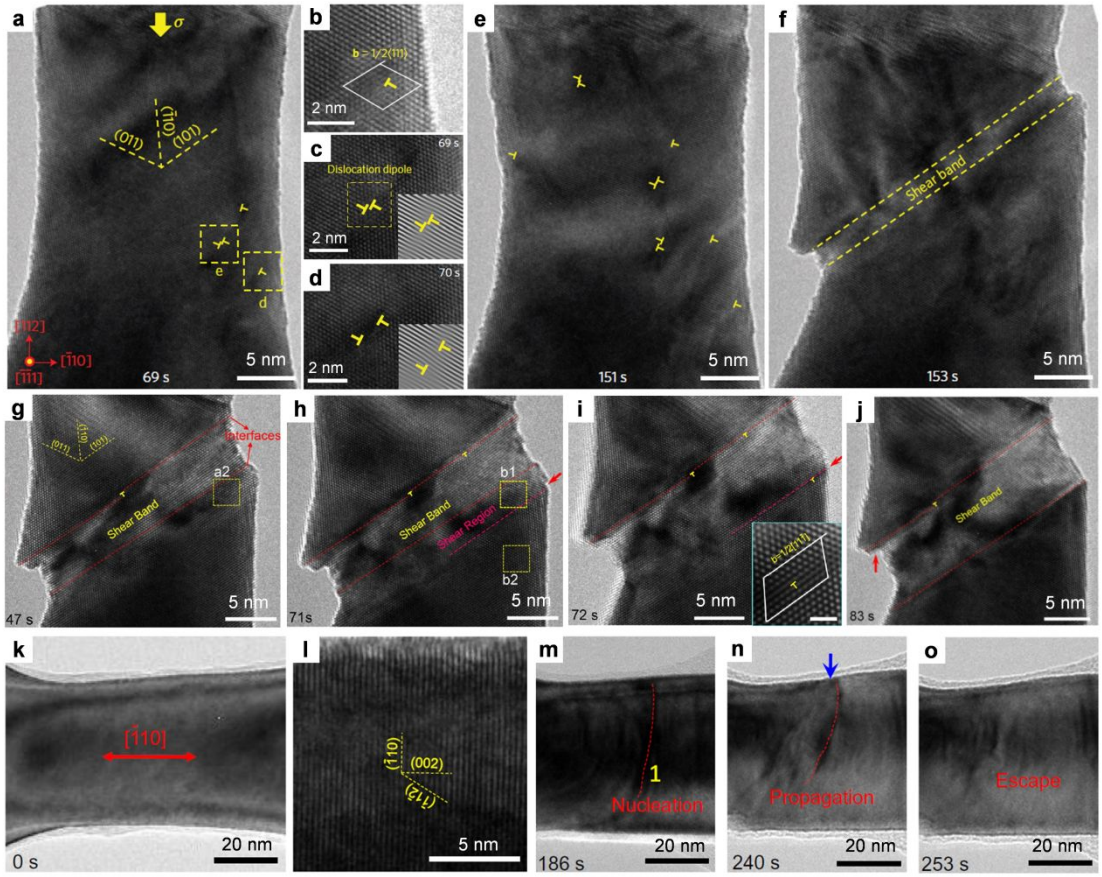

Fig. 4 Dislocation dynamics inside W nanowires at room temperature under a strain rate of 10^{-3} s^{-1}. (a-f) Sequential TEM images showing the deformation of a W bicrystal nanowire (21 nm in diameter) under [112] compression, as viewed along $[\bar{1}\bar{1}1]$, exhibiting the nucleation of dislocations and the formation of a shear band. Dislocations are marked by an upside-down "⊤". (b) Analysis of the Burgers vector indicates a

1/2<111> -type mixed dislocation. (c, d) Sequential TEM images showing the nucleation and expansion of a dislocation dipole under [112] compression. Reproduced with permission from ref. [18], Copyright 2015, Springer Nature. (g) Initial morphology of the shear band with sharp interfaces and atomic-scale steps. (h) Further compression results in a shear region and surface steps (pointed by the red arrow in (h)). (i) A dislocation nucleates from the side surface at the shear region interface (pointed out by the red arrow) and propagates into the crystal. (j) The propagation of dislocations finally induces a new and stable shear band interface, leading to the thickening of shear band. The red arrow indicates the enlargement of surface steps at upper shear band interface. Reproduced with permission from ref. [141], Copyright 2018, Springer Nature. (k-o) Dislocation-dominated plasticity in a 45-nm W nanowire under $[\bar{1}10]$ tension. Under tensile loading, a half-dislocation loop with the Burgers vector of 1/2<111>{110} was emitted from the surface and propagated into the nanowire (m), further loading causes the rotation of the dislocation line around the surface pinning point (n), the dislocation escaped from the surface of the nanowire (o). Reproduced with permission from ref. [142], Copyright 2020, American Association for the Advancement of Science.

3.3 Dislocation-mediated superplastic deformation

Dislocation-mediated superplasticity has been demonstrated in FCC metals via mechanisms such as dislocation slip-activated surface creep[42] and dislocation slip on multiple equivalent slip planes[143]. In contrast, BCC metals typically exhibit high lattice resistance and cross-slip, making these mechanisms difficult to occur[144, 145]. The above section reveals that dislocations can nucleate at the surface and escape under stress. When this phenomenon is sustained, unique phenomena emerge, such as superplastic elongation on BCC nanocrystals[113, 114]. For example, Lu et al.[113] demonstrated that the superplastic elongation strain of BCC Mo single-crystal nanowires exceeds 127% using thermal-bimetallic-based technique (Fig. 5a). They proposed a novel plasticity mechanism of dislocation bubble-like effect, which involves a continuous and homogeneous dislocation nucleation and annihilation. This superplastic behavior is highly related to the size and aspect ratio of the nanowires (Fig. 5b, c). Specifically, they noted that nanowires with diameters greater than 300 nm exhibit poor plastic elongation, while those with diameters less than 300 nm demonstrate improve plasticity, particularly as the aspect ratio decreases (Fig. 5b). In addition, a similar phenomenon was found in the tensile deformation of Ta nanoplates[114] (Fig. 5d, e). These results show that optimizing the structure of BCC metals can effectively enhance their tensile ductility.

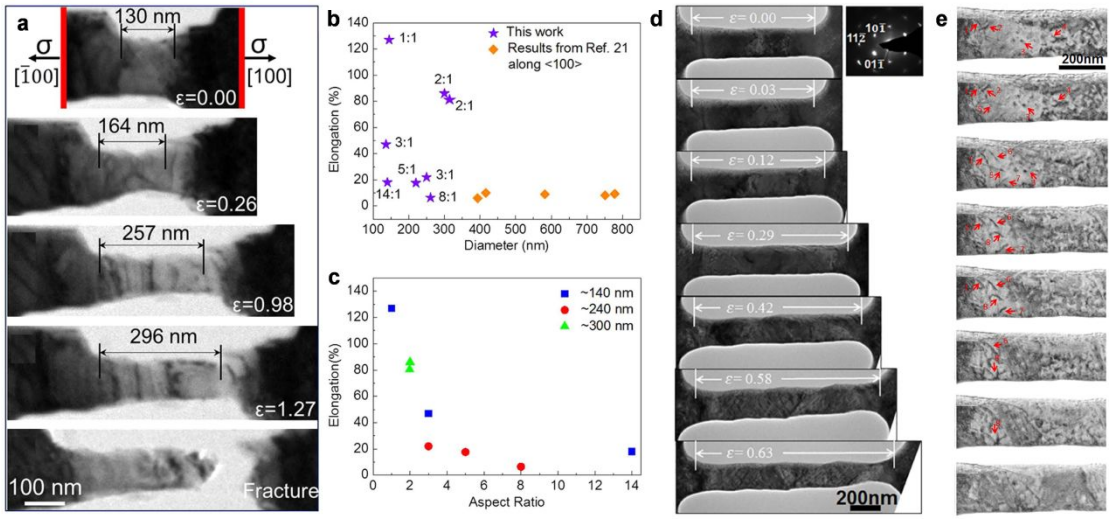

Fig. 5 The super-plastic deformation in BCC nanowires with a strain rate of ~10^{-3} s^{-1} at temperatures below ~60 ℃. (a) A continuous series of bright-field TEM images show the in situ tensile process of a single crystal Mo nanowire that is 135 nm in diameter with an aspect ratio of ~1:1. The tensile strain is nearly along the [100] direction. (b, c) Size effect and aspect ratio on the plastic strain of Mo nanowires. Reproduced with permission from ref. [113], Copyright 2016, Springer Nature. (d, e) A series of TEM images of Ta nanowire exhibits as large as 63% homogenous tensile strain, both the dislocation nucleation and escape process are detected in (e). Reproduced with permission from ref. [114], Copyright 2017, American Institute of Physics.

3.4 Dislocation-mediated ductile fracture

Low fracture toughness has long been a widespread limitation of BCC metals[16, 146, 147], which severely limits their practical applications.

Although many theoretical calculations have investigated the relationship between dislocations and the fracture process[148-150] to enhance the fundamental understanding of toughness and brittleness. However, due to the lack of evidence at the atomic scale, the mechanism of the dynamic interactions between dislocations and crack propagation is unclear. Recently, Lu et al[151] performed in situ atomic-resolution observations of nanoscale fracture in single crystals of BCC Mo using thermal-bimetallic-based technique. They found that the crack growth process involves the nucleation, motion, and interaction of dislocation on multiple 1/2<111 >{ 110} slip system at the crack tip, resulting ductile deformation (Fig. 6a-g) rather than brittle cleavage fracture. They pointed out that the dislocation nucleation at crack tip and the 3D Burgers vector $\boldsymbol{b}$=1/2[111]{1$\bar{1}$0} or 1/2[11$\bar{1}$]{1$\bar{1}$0} (Fig. 6d). In addition, crack-tip dislocations can react with each other to form a dislocation lock with a Burgers vector $\boldsymbol{b}$=[010](100) (Fig. 6e). Fig. 6h show the schematic illustration of two 3D-curved dislocation lines nucleated from the crack tip. These dislocation activities alternately produce crack tip plastic shearing, leading to crack blunting, and localized segregation perpendicular to the crack plane, causing crack extension and sharpening. This result provides insights into the dislocation-mediated mechanisms of the ductile to brittle transition in BCC refractory metals.

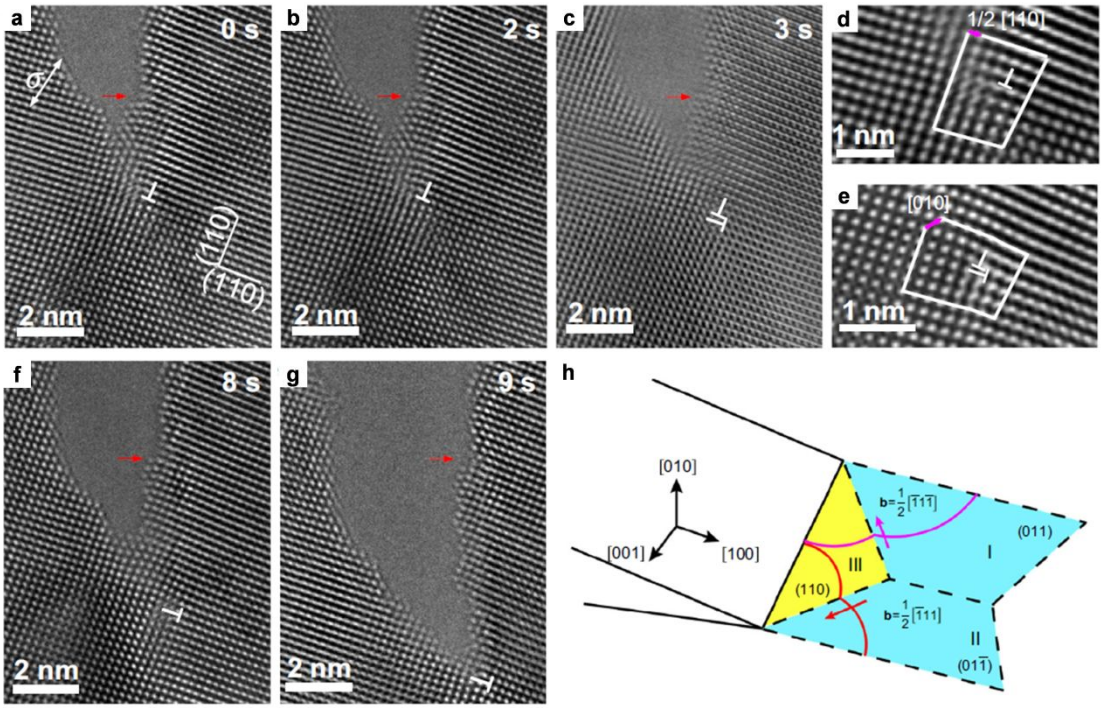

Fig. 6 HRTEM observations of the blunting and growth of a crack due to crack tip dislocation emission at the temperature below 50 ℃. (a-g) A time series of in situ HRTEM images showing crack growth in a Mo nanocrystal, dislocations nucleation, motion and interaction at crack tip, which give rise to an alternation sequence of crack tip plastic shearing. (h) Schematic illustration of two 3D-curved dislocation lines nucleated from the crack tip. The two branches of the pink dislocation line are on slip planes I and III and share the common slip direction $[\bar{1}1\bar{1}]$. The two branches of the red dislocation line are on slip planes II and III and share the common slip direction $[\bar{1}11]$. Reproduced with permission from ref. [151], Copyright 2023, Springer Nature.

4. Twinning deformation in BCC nanocrystals

Deformation twinning is an effective way to achieve ultrahigh strength[51, 152], good ductility[153], and fatigue resistance[154], etc. However, deformation twinning in BCC crystals usually occurs under high strain rates[155] or low temperature[156, 157] in bulk materials. Although numerous theoretical and experimental studies have made progress on the understanding of BCC deformation twinning[158-160], the atomic-scale analysis is still lacking. In small-scale BCC crystals, dislocations and twins become competing deformation modes at room temperature and low strain rates. Twinning could dominate when its nucleation from the surface is easier than that of a dislocation. Based on the sequential fabrication-testing technique, Wang et al.[18] reported the first direct observation of deformation twinning in W nanocrystals with diameters below 20 nm during in situ compression along the <110> direction (Fig. 7a-f). The twin embryo nucleates from the GB or surface, the shear stress is about 9 GPa on the {112} plane. Such deformation twinning is pseudoelastic, and detwinning occurs during unloading. Statistical investigations revealed an evident orientation, size and loading direction dependence of the competition between deformation twinning and dislocation-dominated plasticity[54, 58, 144, 161, 162]. The formation of twinning leads to a change in structural orientation, which can have a significant change on the properties of the metals, such as electro-conductivity[54].

The researcher found that the twin deformation itself is also affected

by size, in addition to the size-mediated transformation of the deformation mode. Zhong et al.[66] revealed the emergence of nucleation- and growth-controlled twinning deformation at different sizes. When the sample is larger than 15 nm in diameter, the deformation exhibits the reluctant twin growth, i.e., the twin growth requires a further increase in stress to achieve twinning, exhibiting growth-controlled deformation twinning (Fig. 7g-j). In contrast, decreasing the diameter below 15 nm avoids reluctant twin growth and leads to nucleation-controlled growth (Fig. 7k-m). The twin structure can quickly get through the cross section of nanocrystals, enabling fast twin growth via the facile migration of the twin boundary (TB). This deformation model difference is associated with the formation of a finite-sized twin structure in relatively large nanocrystals. The screw dislocation-mediated twin nucleation and growth process is further revealed by MD, which shows that screw dislocation can transform into three 1/6<111 >{112} twinning partials on successive {112} layers when stress increased (Fig. 7h). After the twin embryo is produced, the cross-slipped dislocation became three twinning partials on successive {112} layers on a coherent twin boundary (CTB)[59], resulting in the thickening of the twin. This result reveals a close correlation between dislocations and twins. The leading edge of this growing twin embryo consists of twinning partials aligned on successive planes, forming an inclined TB. The formation of inclined TB also leads to the

creation of large amounts of Moiré fringes (MF) in the nanowire (Fig. 7j). The formation of dominant inclined TB with respect to the twinning plane is also a distinguishing feature in BCC metals compared to FCC[163, 164]. One possible reason is the double cross-slip-assisted twinning mechanism[156]. Additionally, unlike high glide velocity of twinning partials in FCC metals, the propagation of twinning partials in BCC metals is very slow, which may also play a key role in formation of the inclined TB. It has been found that the presence of such inclined TB with high interfacial energy that provides the driving force for spontaneous detwinning after stress unloading[54, 165].

Geometric analysis further suggests an anti-twinning mechanism under the reversed loading along the $<110>$ direction[142], the unit slip on the $(\bar{1}1\bar{2})$ plane along $1/3[1\bar{1}\bar{1}]$ dislocation (Fig. 7n-r). This discovery fills a gap in the academic knowledge of anti-twinning behavior and breaks the inherent perception of the plastic deformation behavior of BCC metals. In addition, twinning deformation has also been studied at atomically resolved in coarse BCC materials. The twin lamellae were observed growing inside crystal grains by extruding out of and then expanding with bulges on coherent $\{112\}$ TBs[166]. Since the entire growth process occurs within crystal grains, the influence of the free surface is effectively eliminated. The twin growth process can be described by a self-thickening mechanism driven by dislocation reactions. This growth

process provides insights into deformation twinning in bulk BCC metals.

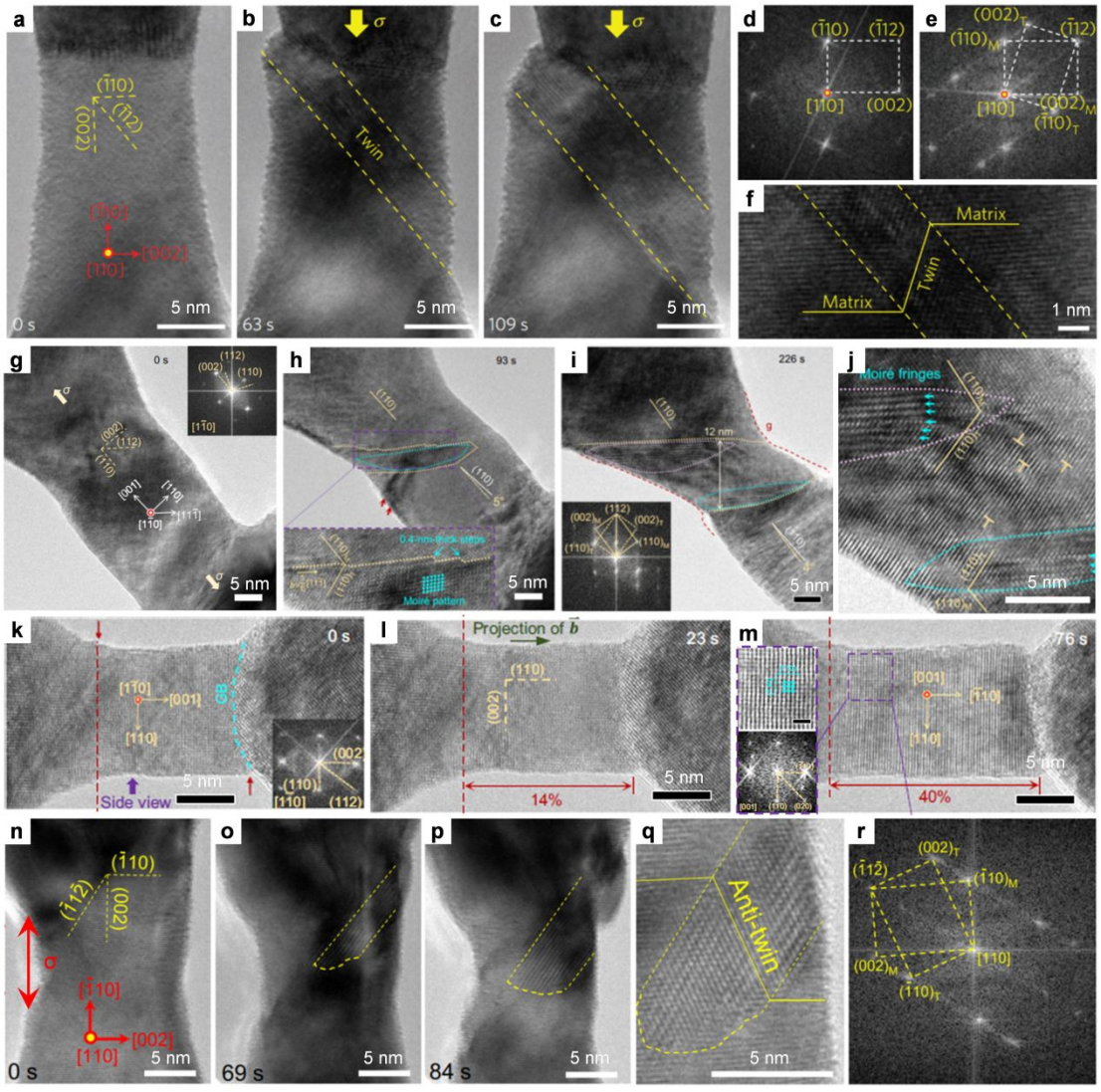

Fig. 7 Mechanistic insight into the deformation mechanism in BCC metallic nanocrystals at room temperature under a strain rate of 10^{-3} s^{-1}. (a-c) Sequential TEM images showing deformation twinning in a W bicrystal nanowire (15 nm in diameter), which is loaded along [$\bar{1}$10] and viewed along [110]. (d, e) Fast Fourier transform pattern of the pristine W bicrystal and the deformation twin. (f) Magnified TEM image showing the deformation twin. Reproduced with permission from ref. [18],

Copyright 2015, Springer Nature. (g-j) Reluctant twin growth in a 23-nm-diameter Ta nanocrystal, twin embryo (inset in h) shows a minimum thickness of six (112) layers at the twin tip. HRTEM image of the deformation twin containing a high density of dislocations. MF were found at both the top and bottom TB (j). (k-m) Large ductility via facile twin thickening in sub-15-nm Ta nanocrystals. Reproduced with permission from ref. [66], Copyright 2024, Springer Nature. (n-r) TEM images showing the deformation-induced anti-twinning in a W bicrystal nanowire (~16 nm in diameter) under $[\bar{1}10]$ tension. Reproduced with permission from ref. [142], Copyright 2018, American Association for the Advancement of Science.

5. Phase transformation mediated deformation

In BCC materials, phase transformation plays a critical role in mediating deformation under various stress conditions[19, 167, 168]. This transformation mechanism enables the material to effectively accommodate external loads, particularly under some extreme conditions. For example, omega (ω) phase transformations and hexagonal (α')/orthorhombic (α") martensitic transformations have been observed in BCC alloys under shock loading[63, 169]. In addition, several phase transformation paths have been predicted, such as BCC-to-FCC[149, 170, 171], BCC-to-hexagonal close-packed (HCP)[172, 173], BCC-to-face-centered

tetragonal (FCT)[174], BCC-to-face-centered orthogonal (FCO)[116]. Phase transformations lead to fundamental structure changes and may dramatically affect the mechanical properties of metals. In recent years, phase transformation has been experimentally validated at the atomic scale during mechanical loading in BCC nanostructures. Wang et al.[19] showed a sequential phase transformation process at a crack tip of Mo thin film at room temperature using a Gatan model 654 straining holder. At the crack tip, the structural transformation was accompanied by shear deformation from an original <001> -oriented BCC structure to a <110> -oriented FCC lattice, and then reverted into <111> -oriented BCC domains (Fig. 8a-f). There were two main reasons for the transformation, on one hand, the extremely high applied shear stress (>7 GPa) could drive the lower energy-state BCC Mo into the high-energy-state FCC Mo; on the other hand, the crack occurred in (010)< 001> , and avoided the twinning relationship in (112)<111> . This phase transformation is often observed during deformation of nanosized BCC metals[113, 115, 144]. Such sequential phase transformation can induce significant lattice rotation to accommodate the plastic deformation of BCC metals. Recently, a new transformation for BCC-FCO has been revealed at room temperature using thermal-bimetallic-based technique[116]. It is pointed out that phase transformation can be achieved via lattice shearing and shuffling. Although phase transformations are

activated under high stresses, and the loading orientation can influence the transition path and resulting phase type. The authors showed that the FCO-structured Mo is a stable phase with a relatively low energy barrier when shear stress is applied along the <110> direction. In contrast, FCC Mo has a high energy barrier, making phase transformation challenging to achieve even under the appropriate loading orientation. With advances in high-temperature in situ nanomechanical testing techniques, Han's group[93] captured the phase transformation process of BCC W at a temperature of 973 K using MEMS-based techniques with a strain resolution of ~10^{-4}. Atomically resolved images of the crack tip successfully confirmed a new insight into the $[100]_{BCC} \rightarrow [110]_{FCC}$ transformation path (Fig. 8g-m). Up to now, many other phase transformations have not been directly verified experimentally. In particular, phase transformation of BCC materials under extreme conditions, such as cryogenic[63], may need to rely on more advanced experimental techniques. At the same time, the fundamental understanding and better control of deformation-induced structure transition are essential to improve the mechanical performances of BCC nanomaterials.

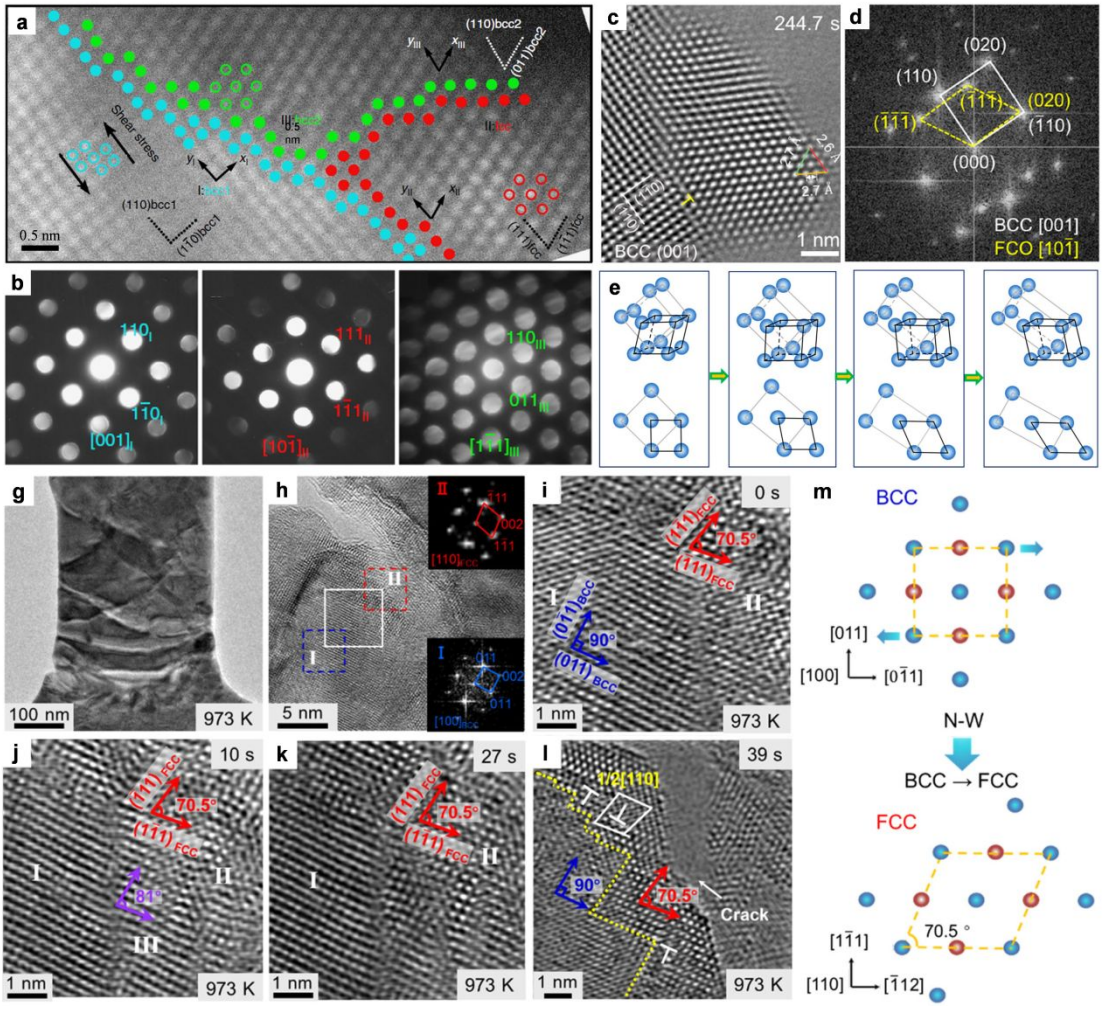

Fig. 8 Phase transformations in BCC nanocrystals. (a) Atomic-resolution HAADF-STEM image showing regions I, II, and III with different crystal structures or orientations. Atoms adjacent to the boundaries between the regions are represented using different colors: blue for the original <001> -BCC1 region, red for the <110> -FCC region, and green for the <111> -BCC2 region. (b) The electron nano diffraction patterns from regions I, II, and III, respectively. Reproduced with permission from ref. [19], Copyright 2014, Springer Nature. (c, d) HRTEM characterization of FCO lattice and the corresponding FFT pattern. (e) The three and two-

dimensional atomic models corresponding to the initial BCC structure, two transition structures, and the final FCO structure of Mo. Reproduced with permission from ref. [116], Copyright 2020, Taylor and Francis Ltd. (g) A TEM bright-field image of the sample at the moment when a crack was initiated upon tensile deformation at 973 K. (h) A HRTEM image of the region around the crack tip. (i-l) Time-resolved HRTEM images of the region within the white box in b showing BCC-FCC phase transformation at the crack tip. (m) A crystallographic schematic of the BCC-FCC phase transformation by habit plane shear of the lattice. Reproduced with permission from ref. [93], Copyright 2021, Springer Nature.

6. Multiple modes mediated deformation

It has been found that all these deformation modes mentioned above are correlated with each other. On the other hand, due to the change of nanowire orientation by dislocation slip, twinning or phase transformation, which can excite other deformation modes during subsequent deformations. Therefore, the deformation process tends to be a coordinated deformation of multiple modes rather than a single deformation mode. Using sequential fabrication-testing technique, Wang et al.[144] uncovered a unique deformation mode on Nb nanowires that can activate phase transformation, deformation twinning, and dislocation slip

under stress (Fig. 9). The occurrence of the phase transformation (Fig. 9b) leads to a change in the orientation of the nanowires, and the newly obtained orientation produces twin deformation upon further loading (Fig. 9c). The dislocation slip-induced change in orientation enables more uniform elongation of the nanowires (Fig. 9d-f). The synergistic effect of these deformation modes leads to a remarkable elongation of more than 269% before fracture in Nb nanowire (Fig. 9g).

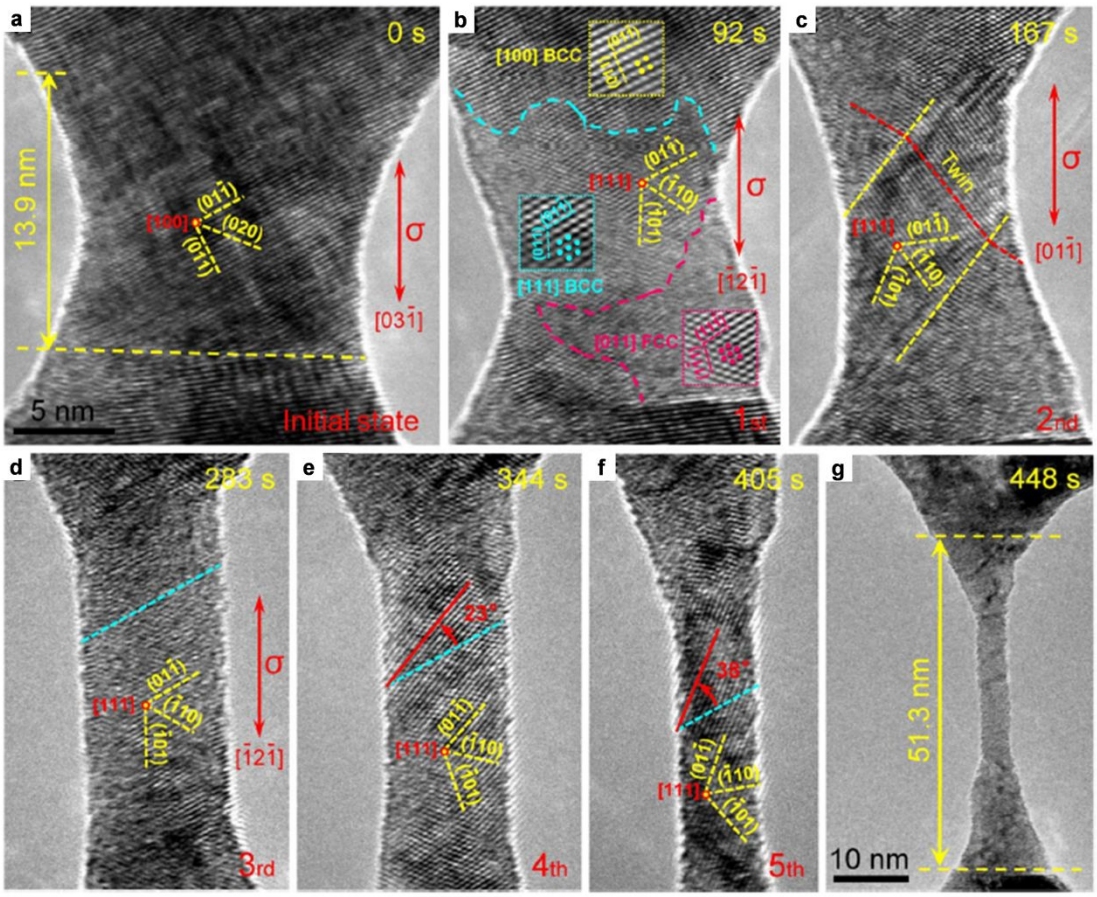

Fig. 9 Deformation-induced multiple reorientations and superplastic deformation in an Nb nanowire at room temperature with a strain rate of 10^{-3} s^{-1}. (a) The pristine Nb nanowire with a diameter of ~13.7 nm and a length of ~13.9 nm. We applied tensile loading along the nanowire axis

of the [$03\bar{1}$] direction. (b) Phase transformation induced reorientation via a two-step BCC-FCC-BCC transition pathway, resulting in a change of the zone axis from [100] to [111] and the nanowire axis from [$03\bar{1}$] to [$\bar{1}2\bar{1}$]. (c) Twinning-mediated second reorientation of the Nb nanowire, resulting in a change of the nanowire axis from [$\bar{1}2\bar{1}$] to [$01\bar{1}$]. (d-f) Correlated reorientations via the slip-induced crystal rotations in the subsequent deformation. (g) After multiple reorientations, the length of the nanowire elongated from 13.9 to 51.3 nm before necking localization, corresponding to a uniform elongation of ~269%. Reproduced with permission from ref. [144], Copyright 2018, American Association for the Advancement of Science.

7. Summary and prospects

This review provides a comprehensive overview of in situ TEM nanomechanical testing techniques and their application in uncovering the deformation mechanisms of BCC nanocrystals. The discussion begins with key nanomechanical testing methods, including classical tensile techniques, nanoindentation, MEMS-based approaches, sequential fabrication-testing techniques, and thermal-bimetallic methods, each offering unique insights into material behavior under different conditions. Then, key deformation mechanisms in BCC nanocrystals, including dislocation activities, twinning deformation, phase transformation-

mediated deformation and the complex interplay between different mechanisms are concluded, emphasizing how in situ TEM has captured their dynamic evolution at atomic resolution. In the following, we will further discuss future challenges and potential opportunities for advancing in situ TEM techniques and their application in studying nanomaterials.

1. The recent advance in TEM techniques, more importantly, ultrahigh-resolution imaging TEM[175] and event-responsive TEM[176], have made it possible to observe the internal structure of different materials, including beam-sensitive materials, at a much higher resolution, and thus relate the properties of the material to the individual atoms[175, 177]. The ultrafast camera for electron detection and data recording is also a key technique[178, 179]. The combination of these techniques is expected to push the limit of the in situ experimental mechanics to the sub-angstrom and millisecond scales, providing new opportunities to capture the ultrafast defect motion in nanostructured materials. However, the use of these technologies has meant an eruption of data in in situ TEM experiments. It is expected that Artificial intelligence (AI), machine learning and deep learning, can automate feature detection, classification, and tracking in TEM data[180].
2. Environment TEM provides a new opportunity to simulate the environment to study the deformation of materials under different

conditions[181, 182], such as controlled temperature[183, 184], atmosphere[185, 186], etc. For example, Shan et al. have done extensive research on the behavior of metals in different atmospheres[186-189]. At the same time, under high temperatures, the dynamic activities are always affected by thermal perturbations at elevated temperatures[190], especially, the effect of hot electrons and thermal drift preventing atomic-scale observation and imaging. Thus, the testing platforms need higher capabilities including high-temperature accurate heating components, mechanical test systems, displacement drives, and multichannel signal transmission[191, 192]. Low-temperature environments, typically achieved by cooling to liquid helium or liquid nitrogen temperatures, are widely used in classical tensile techniques to study dislocation behaviors[120, 193]. Consistent with room temperature conditions, nanoscale BCC metals may be more susceptible to twinning and phase transitions at low temperatures due to elevated stress levels. The interaction of these mechanisms may enhance the strength and ductility of BCC metals at low temperatures.

3. Three-dimensional (3D) technology, such as electron tomography, has a huge advantage over two-dimensional (2D) projections on characterization for dislocations, domains, phase structures, and amorphous structures[53, 194, 195]. Especially in the last two decades, the development of advanced recording devices and aberration-corrected

electron microscopy, pushes the resolution of electron tomography to the atomic level[196]. This is of great significance for the characterization of some structured materials, such as TB[154, 197-199], and GB[96, 200-202]. Recently, Huang et al.[203] tracked the rotations of individual grains in nanograined nickel by using 3D orientation mapping in TEM before and after in situ nanomechanical testing. They found that many of the larger-size grains underwent unexpected lattice rotations. These results provide insights into the fundamental deformation mechanisms of nanograined metals and will help to guide strategies for material design and engineering applications.

4. Crystal structures have a great influence on mechanical properties[51, 204], so, understanding the deformation of different structures is of certain guiding significance for the controllable preparation of nanomaterials with special structures. For nanotwinned materials, such as twin-twin intersection mechanical behavior[102] and 3D nanotwins[205] showed high strength coupled with high ductility and continuous strain hardening. Besides, structural materials adopted in practical applications usually take advantage of a combination of multiple elements (such as alloys[206, 207]) and complex microstructures (such as multiple phases[208], hierarchical structures[164, 209], and metallic glass[210]). Therefore, revealing the deformation process of materials with different nanocrystal structures can help to design materials with

excellent mechanical properties.

5. Quantitative measurement of nanoscale mechanical properties is challenging. Currently, most reported mechanical properties are achieved from MD simulations[18, 19], which lack experimental data. Although AFM cantilever have been integrated into MEMS[211], the transfer process can introduce damage or surface contamination[134, 212]. Therefore, machining customized AFM cantilevers is beneficial for achieving accurate testing of mechanical properties. For instance, employing a sequential fabrication-testing technique to customize cantilevers from various materials enables both high-quality nanowire preparation and accurate measurement of mechanical properties.
6. In addition, some emerging fields such as nanotribology urgently need to understand the characterization of interfaces through in situ TEM[213-215]. Wang et al.[214] unveiled the atomic-scale friction of a single W asperity in real time through the HRTEM investigation of a nanocontact in countermotion. Compared to macroscopic tribology, the construction of these in situ experiments to elucidate the dynamics of atomic friction not only helps to explain friction mechanisms on an atomic scale but also guides in atomic-scale manufacturing.

In conclusion, in situ TEM nanomechanical testing have achieved important results in revealing the deformation mechanism of nanosized

BCC materials, which is of great significance in enriching the study of metal deformation mechanisms. These in situ investigations in turn provide valuable guidance for the realization of high-quality nanostructures and M/NEMS by inducing structural design in a controlled manner. In the near future, we believe that the in situ mechanical TEM method will continue to evolve, offering unprecedented capabilities to resolve dynamic processes in advanced materials in more realistic environments. Thus, it can offer promising possibilities for practical applications, which is more in line with the importance of scientific research.

Author contributions

Hai Li, Li Zhong: conceptualization, formal analysis, and writing – original draft. Ming Sheng, Kailin Luo, Min Liu, Qiuyang Tan: writing – review & editing. Sijing Chen, Li Zhong, Litao Sun: supervision, writing – review & editing, and funding acquisition.

Data availability

No primary research results, software or code have been included and no new data were generated or analyzed as part of this review.

Conflicts of interest

There are no conflicts to declare.

Acknowledgements

This work was supported by the National Key R&D Program of China under Grants No. 2020YFB2007400, the National Natural Science Foundation of China (Grant No. T2321002 and 52271142), the Natural Science Foundation of Jiangsu Province (BK20230028), the Fundamental Research Funds for the Central Universities, the National Natural Science Foundation of China (52401006), the Basic Research Program of Jiangsu Province (NO. BK20230863), the National Science Foundation for Post-doctoral Scientists of China (NO. 2023M730550).

References

1. L. Vocadlo, D. Alfe, M. Gillan, I. Wood, J. Brodholt and G. Price, *Nature*, 2003, **424**, 536-539.
2. T. Zhu and J. Li, *Prog. Mater Sci.*, 2010, **55**, 710-757.
3. T. Tsuru, S. Han, S. Matsuura, Z. Chen, K. Kishida, I. Iobzenko, S. I. Rao, C. Woodward, E. P. George and H. Inui, *Nat Commun*, 2024, **15**, 1706.
4. S. A. Kube, C. Frey, C. McMullin, B. Neuman, K. M. Mullin and T. M. Pollock, *Acta Mater.*, 2024, **265**, 119628.
5. N. Parkes, R. Dodds, A. Watson, D. Dye, C. Hardie, S. A. Humphry-Baker and A. J. Knowles, *Int. J. Refract. Met. Hard Mater*, 2023, **113**, 106209.
6. R. Maaß, S. Van Petegem, D. Ma, J. Zimmermann, D. Grolimund, F. Roters, H. Van Swygenhoven and D. Raabe, *Acta Mater.*, 2009, **57**, 5996-6005.
7. W. Z. Han, L. Huang, S. Ogata, H. Kimizuka, Z. C. Yang, C. Weinberger, Q. J. Li, B. Y. Liu, X. X. Zhang, J. Li, E. Ma and Z. W. Shan, *Adv. Mater.*, 2015, **27**, 3385-3390.
8. A. E. Lita, D. Rosenberg, S. Nam, A. J. Miller, D. Balzar, L. M. Kaatz and R. E. Schwall, *IEEE Trans. Appl. Supercond.*, 2005, **15**, 3528-3531.
9. Y. Lee, C. Choi, Y. Jang, E. Kim, B. Ju, N. Min and J. Ahn, *Appl. Phys. Lett.*, 2002, **81**, 745-747.
10. L. L. Rajeswara Rao, M. K. Singha, K. M. Subramaniam, N. Jampana and S. Asokan, *IEEE*

Sens. J., 2017, **17**, 22-29.
11. L. Ni, R. M. Pocratsky and M. P. de Boer, *Microsyst. Nanoeng.*, 2021, **7**, 1-13.
12. I. Erofeev, A. W. Hartanto, K. Saidov, Z. Aabdin, A. Pacco, H. Philipsen, W. W. Tjiu, H. K. Hui, F. Holsteyns and U. Mirsaidov, *Adv. Electron. Mater.*, 2024, 2400035.
13. K. Saidov, I. Erofeev, Z. Aabdin, A. Pacco, H. Philipsen, A. W. Hartanto, Y. Chen, H. Yan, W. W. Tjiu, F. Holsteyns and U. Mirsaidov, *Adv. Funct. Mater.*, 2023, **34**, 2310838.
14. L. Ni and M. P. de Boer, *J. Microelectromech. Syst.*, 2021, **30**, 426-432.
15. L. Ni and M. P. de Boer, *J. Microelectromech. Syst.*, 2022, **31**, 167-175.
16. J. Kim, D. Jang and J. R. Greer, *Acta Mater.*, 2010, **58**, 2355-2363.
17. J. Y. Kim, D. Jang and J. R. Greer, *Int. J. Plast.*, 2012, **28**, 46-52.
18. J. Wang, Z. Zeng, C. R. Weinberger, Z. Zhang, T. Zhu and S. X. Mao, *Nat. Mater.*, 2015, **14**, 594-600.
19. S. J. Wang, H. Wang, K. Du, W. Zhang, M. L. Sui and S. X. Mao, *Nat. Commun.*, 2014, **5**, 3433.
20. A. Dutta, M. Bhattacharya, P. Barat, P. Mukherjee, N. Gayathri and G. C. Das, *Phys. Rev. Lett.*, 2008, **101**, 115506.
21. C. J. Healy and G. J. Ackland, *Acta Mater.*, 2014, **70**, 105-112.
22. D. Caillard, *Acta Mater.*, 2010, **58**, 3493-3503.
23. Y. Lu, X. Shu and X. Liao, *Sci. China Mater.*, 2018, **61**, 1495-1516.
24. J. R. Greer and J. T. M. De Hosson, *Prog. Mater Sci.*, 2011, **56**, 654-724.
25. C. R. Weinberger and W. Cai, *J. Mater. Chem.*, 2012, **22**, 3277.
26. V. Vitek, *Philos. Mag.*, 2004, **84**, 415-428.
27. A. Seeger and U. Holzwarth, *Philos. Mag.*, 2006, **86**, 3861-3892.
28. J. Christian, *Metall. Mater. Trans. A-Phys. Metall. Mater. Sci.*, 1983, **14**, 1237-1256.
29. C. R. Weinberger, B. L. Boyce and C. C. Battaile, *Int. Mater. Rev.*, 2013, **58**, 296-314.
30. Z. Pan, Y. Li and Q. Wei, *Acta Mater.*, 2008, **56**, 3470-3480.
31. A. Cao, *J. Appl. Phys.*, 2010, **108**, 113531.
32. X. Li, Y. Wei, L. Lu, K. Lu and H. Gao, *Nature*, 2010, **464**, 877-880.
33. P. Wang, W. Chou, A. Nie, Y. Huang, H. Yao and H. Wang, *J. Appl. Phys.*, 2011, **110**, 093521.
34. J. Zhu and D. Shi, *J. Phys. D: Appl. Phys.*, 2011, **44**, 055404.
35. G. Sainath and B. K. Choudhary, *Comput. Mater. Sci*, 2016, **111**, 406-415.
36. S. Kotrechko, A. Timoshevskii, I. Mikhailovskij, T. Mazilova, N. Stetsenko, O. Ovsijannikov and V. Lidych, *Eng. Fract. Mech.*, 2015, **150**, 184-196.
37. J. J. Bian, L. Yang, X. R. Niu and G. F. Wang, *Philos. Mag.*, 2018, **98**, 1848-1864.
38. A. H. M. Faisal and C. R. Weinberger, *Comput. Mater. Sci*, 2024, **233**.
39. H. Van Swygenhoven and J. R. Weertman, *Mater. Today*, 2006, **9**, 24-31.
40. S. Tateyama, Y. Shibuta and T. Suzuki, *Scr. Mater.*, 2008, **59**, 971-974.
41. S. Ogata, Y. Umeno and M. Kohyama, *Modell. Simul. Mater. Sci. Eng.*, 2009, **17**, 013001.
42. L. Zhong, F. Sansoz, Y. He, C. Wang, Z. Zhang and S. X. Mao, *Nat. Mater.*, 2017, **16**, 439-445.
43. S. D. Sun, D. L. Kong, D. H. Li, X. Liao, D. Liu, S. Mao, Z. Zhang, L. Wang and X. Han, *ACS Nano*, 2019, **13**, 8708-8716.
44. Q. Yu, M. Legros and A. M. Minor, *MRS Bull.*, 2015, **40**, 62-70.

45. H. D. Espinosa, R. A. Bernal and T. Filleter, *Small*, 2012, **8**, 3233-3252.
46. M. Legros, *C.R. Phys.*, 2014, **15**, 224-240.
47. C. Luo, C. Wang, X. Wu, J. Zhang and J. Chu, *Small*, 2017, **13**, 1604259.
48. L. T. Sun, T. Xu and Z. Zhang, In-situ transmission electron microscopy, *Springer*, 2023.
49. K. Li, Y. Bu and H. Wang, *Front. Mater.*, 2023, **10**, 1207024.
50. C. Liu, K. Yang, J. Zhang, S. Cheng and C. Shan, *Microstructures*, 2024, **4**, 2024055.
51. J. W. Wang, F. Sansoz, J. Huang, Y. Liu, S. Sun, Z. Zhang and S. X. Mao, *Nat. Commun.*, 2013, **4**, 1742.
52. D. Xie, S. Li, M. Li, Z. Wang, P. Gumbsch, J. Sun, E. Ma, J. Li and Z. Shan, *Nat. Commun.*, 2016, **7**, 13341.
53. B. Liu, F. Liu, N. Yang, X. Zhai, L. Zhang, Y. Yang, B. Li, J. Li, E. Ma, J. Nie and Z. Shan, *Science*, 2019, **365**, 73-75.
54. H. Peng, Y. Hou, W. Meng, H. Zheng, L. Zhao, Y. Zhang, K. Li, P. Zhao, T. Liu, S. Jia and J. Wang, *Small*, 2023, **19**, 2206380.
55. M. Kühne, F. Börrnert, S. Fecher, M. Ghorbani-Asl, J. Biskupek, D. Samuelis, A. V. Krasheninnikov, U. Kaiser and J. H. Smet, *Nature*, 2018, **564**, 234-239.
56. Z. Zhang, N. Liu, L. Li, J. Su, P. Chen, W. Lu, Y. Gao and J. Zou, *Nano Lett.*, 2018, **18**, 6597-6603.
57. J. Sun, L. He, Y. C. Lo, T. Xu, H. Bi, L. Sun, Z. Zhang, S. X. Mao and J. Li, *Nat. Mater.*, 2014, **13**, 1007-1012.
58. L. Zhao, G. Chen, H. Zheng, S. Jia, K. Li, R. Jiang, L. Li, Y. Zhang, H. Peng, P. Zhao, Z. Huang and J. Wang, *J. Mater. Sci. Technol.*, 2023, **144**, 235-242.
59. J. Wang, A. H. M. Faisal, X. Li, Y. Hong, Q. Zhu, H. Bei, Z. Zhang, S. X. Mao and C. R. Weinberger, *J. Mater. Sci. Technol.*, 2022, **106**, 33-40.
60. J. S. Koehler, M. Cohen, F. Seitz, W. T. Read, W. Shockley and E. Orowan, Dislocations in metals, *American Institute of Mining*, 1954.
61. X. Li, Z. Zhang and J. Wang, *Prog. Mater Sci.*, 2023, **139**, 101160.
62. L. Hsiung and D. Lassila, *Acta Mater.*, 2000, **48**, 4851-4865.
63. X. Li, Q. Zhao, Q. Wang, Y. Tian, H. Zhou and J. Wang, *Mater. Res. Lett.*, 2021, **9**, 523-530.
64. X. Li, Q. Zhao, Y. Tian, Q. Wang, J. Fan, K. Song, H. Zhou and J. Wang, *Acta Mater.*, 2023, **249**.
65. A. Mostafa, L. Vu, Z. Guo, A. K. Shargh, A. Dey, H. Askari and N. Abdolrahim, *Comput. Mater. Sci*, 2024, **244**, 113273.
66. L. Zhong, Y. Zhang, X. Wang, T. Zhu and S. X. Mao, *Nat. Commun.*, 2024, **15**, 560.
67. J. Marian, W. Cai and V. V. Bulatov, *Nat. Mater.*, 2004, **3**, 158-163.
68. A. Couret, J. Crestou, S. Farenc, G. Molenat, N. Clement, A. Coujou and D. Caillard, *Microsc. Microanal. Microstruct.*, 1993, **4**, 153-170.
69. Z. Shan, E. Stach, J. Wiezorek, J. Knapp, D. Follstaedt and S. Mao, *Science*, 2004, **305**, 654-657.
70. Y. Wang, Z. Guo, R. Ma, G. Hao, Y. Zhang, J. Lin and M. Sui, *Prog. Nat. Sci.: Mater. Int.*, 2014, **24**, 121-127.
71. F. Mompiou, M. Legros, A. Boé, M. Coulombier, J. P. Raskin and T. Pardoen, *Acta Mater.*, 2013, **61**, 205-216.
72. Z. Zhang, M. M. Mao, J. Wang, B. Gludovatz, Z. Zhang, S. X. Mao, E. P. George, Q. Yu and

R. O. Ritchie, *Nat. Commun.*, 2015, **6**, 10143.
73. M. Legros, D. S. Gianola and K. J. Hemker, *Acta Mater.*, 2008, **56**, 3380-3393.
74. Z. W. Shan, E. A. Stach, J. M. K. Wiezorek, J. A. Knapp, D. M. Follstaedt and S. X. Mao, *Science*, 2004, **305**, 654-657.
75. M. Wall and U. Dahmen, *Microsc. Res. Tech.*, 1998, **42**, 248-254.
76. E. A. Stach, T. Freeman, A. M. Minor, D. K. Owen, J. Cumings, M. A. Wall, T. Chraska, R. Hull, J. W. Morris, A. Zettl and U. Dahmen, *Microsc. Microanal.*, 2002, **7**, 507-517.
77. W. C. Oliver and G. M. Pharr, *J. Mater. Res.*, 1992, **7**, 1564-1583.
78. J. B. Pethicai, R. Hutchings and W. C. Oliver, *Philos. Mag. A*, 1983, **48**, 593-606.
79. A. M. Minor, S. A. Asif, Z. Shan, E. A. Stach, E. Cyrankowski, T. J. Wyrobek and O. L. Warren, *Nat. Mater.*, 2006, **5**, 697-702.
80. J. Y. Huang, H. Zheng, S. X. Mao, Q. Li and G. T. Wang, *Nano Lett.*, 2011, **11**, 1618-1622.
81. R. J. Milne, A. J. Lockwood and B. J. Inkson, *J. Phys. D: Appl. Phys.*, 2011, **44**, 485301.
82. D. Ge, A. M. Minor, E. A. Stach and J. W. Morris, *Philos. Mag.*, 2006, **86**, 4069-4080.
83. D. Zhang, L. Jiang, X. Wang, I. J. Beyerlein, A. M. Minor, J. M. Schoenung, S. Mahajan and E. J. Lavernia, *J. Mater. Res.*, 2019, **34**, 1499-1508.
84. S. Lee, J. Jeong, Y. Kim, S. M. Han, D. Kiener and S. H. Oh, *Acta Mater.*, 2016, **110**, 283-294.
85. C. Q. Dang, J. P. Chou, B. Dai, C. Chou, Y. Yang, R. Fan, W. Lin, F. Meng, A. Hu, J. Zhu, J. Han, A. Minor, J. Li and Y. Lu, *Science*, 2021, **371**, 76-78.
86. M. Haque and M. Saif, *Exp. Mech.*, 2002, **42**, 123-128.
87. L. Y. Chen, M. R. He, J. Shin, G. Richter and D. S. Gianola, *Nat. Mater.*, 2015, **14**, 707-713.
88. T. Ishida, Y. Nakajima, K. Kakushima, M. Mita, H. Toshiyoshi and H. Fujita, *J. Micromech. Microeng.*, 2010, **20**, 075011.
89. T. Sato, L. Jalabert and H. Fujita, *Microelectron. Eng.*, 2013, **112**, 269-272.
90. Y. Zhu and H. Espinosa, *PNAS*, 2005, **102**, 14503-14508.
91. Y. Lu, Y. Ganesan and J. Lou, *Exp. Mech.*, 2009, **50**, 47-54.
92. H. Guo, K. Chen, Y. Oh, K. Wang, C. Dejoie, S. A. Syed Asif, O. L. Warren, Z. W. Shan, J. Wu and A. M. Minor, *Nano Lett.*, 2011, **11**, 3207-3213.
93. J. F. Zhang, Y. R. Li, X. C. Li, Y. Zhai, Q. Zhang, D. Ma, S. Mao, Q. Deng, Z. Li, X. Li, X. Wang, Y. Liu, Z. Zhang and X. Han, *Nat. Commun.*, 2021, **12**, 2218.
94. H. Zheng, A. Cao, C. R. Weinberger, J. Y. Huang, K. Du, J. Wang, Y. Ma, Y. Xia and S. X. Mao, *Nat. Commun.*, 2010, **1**, 144.
95. H. Zheng, J. Wang, J. Y. Huang, J. Wang and S. X. Mao, *Nanoscale*, 2014, **6**, 9574-9578.
96. Q. Zhu, Q. Huang, C. Guang, X. An, S. X. Mao, W. Yang, Z. Zhang, H. Gao, H. Zhou and J. Wang, *Nat. Commun.*, 2020, **11**, 3100.
97. N. Li, J. Wang, A. Misra, X. Zhang, J. Y. Huang and J. P. Hirth, *Acta Mater.*, 2011, **59**, 5989-5996.
98. R. Shao, S. Chen, Z. Dou, J. Zhang, X. Ma, R. Zhu, J. Xu, P. Gao and D. Yu, *Nano Lett.*, 2018, **18**, 6094-6099.
99. J. Huang, L. Zhong, C. Wang, J. Sullivan, W. Xu, L. Zhang, S. Mao, N. Hudak, X. Liu, A. Subramanian, H. Fan, L. Qi, A. Kushima and J. Li, *Science*, 2010, **330**, 1515-1520.
100. Z. Yang, P. V. Ong, Y. He, L. Wang, M. E. Bowden, W. Xu, T. C. Droubay, C. Wang, P. V. Sushko and Y. Du, *Small*, 2018, **14**, 1803108.

101. L. Zhong, J. W. Wang, H. W. Sheng, Z. Zhang and S. X. Mao, *Nature*, 2014, **512**, 177-180.
102. S. Zhao, Q. Zhu, X. An, H. Wei, K. Song, S. X. Mao and J. Wang, *J. Mater. Sci. Technol.*, 2020, **53**, 118-125.
103. Chinese Pat*.,* No. 200610144031.x., 2009.
104. L. H. Wang, T. J. Xin, D. L. Kong, X. Shu, Y. Chen, H. Zhou, J. Teng, Z. Zhang, J. Zou and X. Han, *Scr. Mater.*, 2017, **134**, 95-99.
105. X. D. Han, L. H. Wang, P. Liu, Y. H. Yue, M. J. Yang, J. L. Sun and Z. Zhang, *Mater. Sci. Forum*, 2010, **654-656**, 2293-2296.
106. L. H. Wang, J. Teng, P. Liu, A. Hirata, E. Ma, Z. Zhang, M. Chen and X. Han, *Nat. Commun.*, 2014, **5**, 4402.
107. D. Li, X. Shu, D. Kong, H. Zhou and Y. Chen, *J. Mater. Sci. Technol.*, 2018, **34**, 2027-2034.
108. L. H. Wang, X. D. Han, P. Liu, Y. Yue, Z. Zhang and E. Ma, *Phys. Rev. Lett.*, 2010, **105**, 135501.
109. L. Wang, Z. Zhang, E. Ma and X. D. Han, *Appl. Phys. Lett.*, 2011, **98**, 051905.
110. P. Liu, S. C. Mao, L. H. Wang, X. D. Han and Z. Zhang, *Scr. Mater.*, 2011, **64**, 343-346.
111. Y. H. Yue, P. Liu, Z. Zhang, X. Han and E. Ma, *Nano Lett.*, 2011, **11**, 3151-3155.
112. L. Wang, D. Kong, Y. Zhang, L. Xiao, Y. Lu, Z. Chen, Z. Zhang, J. Zou, T. Zhu and X. Han, *ACS Nano*, 2017, **11**, 12500-12508.
113. Y. Lu, S. Xiang, L. Xiao, L. Wang, Q. Deng, Z. Zhang and X. Han, *Sci. Rep.*, 2016, **6**, 22937.
114. Y. Ma, Y. Lu, D. Kong, X. Shu, Q. Deng, H. Zhou, Y. Chen, J. Zou and L. Wang, *AIP Adv.*, 2017, **7**, 045218.
115. Y. Lu, X. Shu, Z. Li, H. Long, D. Kong, S. Sun, Q. Deng, Y. Chen, Z. Hu, L. Wang and X. Han, *J. Alloys Compd.*, 2019, **806**, 283-291.
116. Y. Lu, S. Sun, Y. Zeng, Q. Deng, Y. Chen, Y. Li, X. Li, L. Wang and X. Han, *Mater. Res. Lett.*, 2020, **8**, 348-355.
117. Y. F. Zhang, X. D. Han, K. Zheng, Z. Zhang, X. Zhang, J. Fu, Y. Ji, Y. Hao, X. Guo and Z. L. Wang, *Adv. Funct. Mater.*, 2007, **17**, 3435-3440.
118. J. Liu, C. Chen, Q. Feng, X. Fang, H. Wang, F. Liu, J. Lu and D. Raabe, *Mater. Sci. Eng., A*, 2017, **703**, 236-243.
119. C. Chisholm, H. Bei, M. B. Lowry, J. Oh, S. A. Syed Asif, O. L. Warren, Z. W. Shan, E. P. George and A. M. Minor, *Acta Mater.*, 2012, **60**, 2258-2264.
120. D. Caillard, B. Bienvenu and E. Clouet, *Nature*, 2022, **609**, 936-941.
121. L. Proville and A. Choudhury, *Nat. Mater.*, 2024, **23**, 47-51.
122. N. Bertin, W. Cai, S. Aubry, A. Arsenlis and V. V. Bulatov, *Acta Mater.*, 2024, **271**, 119884.
123. J. Kim, D. Jang and J. R. Greer, *Scr. Mater.*, 2009, **61**, 300-303.
124. A. S. Schneider, D. Kaufmann, B. G. Clark, C. P. Frick, P. A. Gruber, R. Monig, O. Kraft and E. Arzt, *Phys. Rev. Lett.*, 2009, **103**, 105501.
125. O. Torrents Abad, J. M. Wheeler, J. Michler, A. S. Schneider and E. Arzt, *Acta Mater.*, 2016, **103**, 483-494.
126. J. Hutchinson, *Int. J. Solids Struct.*, 2000, **37**, 225-238.
127. C. Weinberger and W. Cai, *PNAS*, 2008, **105**, 14304-14307.
128. S. H. Oh, M. Legros, D. Kiener and G. Dehm, *Nat. Mater.*, 2009, **8**, 95-100.
129. W. D. Nix, J. R. Greer, G. Feng and E. T. Lilleodden, *Thin Solid Films*, 2007, **515**, 3152-3157.

130. J. R. Greer and W. D. Nix, *Phys. Rev. B*, 2006, **73**, 245410.
131. A. Cao, Y. Wei and S. X. Mao, *Scr. Mater.*, 2008, **59**, 219-222.
132. Z. W. Shan, R. K. Mishra, S. A. Syed Asif, O. L. Warren and A. M. Minor, *Nat. Mater.*, 2008, **7**, 115-119.
133. S. Brinckmann, J. Y. Kim and J. R. Greer, *Phys. Rev. Lett.*, 2008, **100**, 155502.
134. K. Y. Xie, S. Shrestha, Y. Cao, P. J. Felfer, Y. Wang, X. Liao, J. M. Cairney and S. P. Ringer, *Acta Mater.*, 2013, **61**, 439-452.
135. S. Min Han, G. Feng, J. Young Jung, H. Joon Jung, J. R. Groves, W. D. Nix and Y. Cui, *Appl. Phys. Lett.*, 2013, **102**, 041910.
136. L. Huang, Q. J. Li, Z. W. Shan, J. Li, J. Sun and E. Ma, *Nat. Commun.*, 2011, **2**, 547.
137. S. M. Han, T. Bozorg-Grayeli, J. R. Groves and W. D. Nix, *Scr. Mater.*, 2010, **63**, 1153-1156.
138. J. R. Greer, C. R. Weinberger and W. Cai, *Mater. Sci. Eng., A*, 2008, **493**, 21-25.
139. I. Ryu, W. D. Nix and W. Cai, *Acta Mater.*, 2013, **61**, 3233-3241.
140. M. Monavari and M. Zaiser, *Mater. Theory*, 2018, **2**, 3.
141. J. Wang, Y. Wang, W. Cai, J. Li, Z. Zhang and S. X. Mao, *Sci. Rep.*, 2018, **8**, 4574.
142. J. Wang, Z. Zeng, M. Wen, Q. Wang, D. Chen, Y. Zhang, P. Wang, H. Wang, Z. Zhang, S. Mao and T. Zhu, *Sci. Adv.*, 2020, **6**, eaay2792.
143. G. Cao, J. W. Wang, K. Du, X. Wang, J. Li, Z. Zhang and S. X. Mao, *Adv. Funct. Mater.*, 2018, **28**, 1805258.
144. Q. N. Wang, J. W. Wang, J. X. Li, Z. Zhang and S. Mao, *Sci. Adv.*, 2018, **4**, 1-7.
145. S. Davydov, *Phys. Solid State*, 1999, **41**, 8-10.
146. Z. Zhao and F. Chu, *Mater. Sci. Eng., A*, 2017, **707**, 81-91.
147. L. Zhang, G. Csányi, E. van der Giessen and F. Maresca, *npj Comput. Mater.*, 2023, **9**, 217.
148. C. H. Ersland, I. R. Vatne and C. Thaulow, *Modell. Simul. Mater. Sci. Eng.*, 2012, **20**, 075004.
149. I. Ringdalen Vatne, A. Stukowski, C. Thaulow, E. Østby and J. Marian, *Mater. Sci. Eng., A*, 2013, **560**, 306-314.
150. D. Terentyev, E. E. Zhurkin and G. Bonny, *Comput. Mater. Sci*, 2012, **55**, 313-321.
151. Y. Lu, Y. Chen, Y. Zeng, Y. Zhang, D. Kong, X. Li, T. Zhu, X. Li, S. Mao, Z. Zhang, L. Wang and X. Han, *Nat. Commun.*, 2023, **14**, 5540.
152. K. Lu, L. Lu and S. Suresh, *Science*, 2009, **324**, 349-352.
153. L. Lu, Y. Shen, X. Chen, L. Qian and K. Lu, *Science*, 2004, **304**, 422-426.
154. L. L. Li, Z. J. Zhang, P. Zhang, Z. G. Wang and Z. F. Zhang, *Nat. Commun.*, 2014, **5**, 3536.
155. L. A. Zepeda Ruiz, A. Stukowski, T. Oppelstrup and V. V. Bulatov, *Nature*, 2017, **550**, 492-495.
156. C. Q. Chen, J. N. Florando, M. Kumar, K. T. Ramesh and K. J. Hemker, *Acta Mater.*, 2014, **69**, 114-125.
157. Y. T. Zhu, X. Z. Liao and X. L. Wu, *Prog. Mater Sci.*, 2012, **57**, 1-62.
158. Y. Zhang, P. C. Millett, M. Tonks and S. B. Biner, *Acta Mater.*, 2012, **60**, 6421-6428.
159. L. Liu, H. C. Wu, J. Wang, S. K. Gong and S. X. Mao, *Philos. Mag. Lett.*, 2014, **94**, 225-232.
160. S. Goel, B. Beake, C.-W. Chan, N. Haque Faisal and N. Dunne, *Mater. Sci. Eng., A*, 2015, **627**, 249-261.
161. S. Wei, Q. Wang, H. Wei and J. Wang, *Mater. Res. Lett.*, 2019, **7**, 210-216.
162. H. Peng, Y. Hou, H. Zheng, L. Zhao, Y. Zhang, W. Meng, T. Liu, P. Zhao, S. Jia and J. Wang, *J. Mater. Sci. Technol.*, 2023, **154**, 107-113.

163. Q. Zhu, L. Kong, H. Lu, Q. Huang, Y. Chen, Y. Liu, W. Yang, Z. Zhang, F. Sansoz, H. Zhou and J. Wang, *Sci. Adv.*, 2021, **7**, 4758.
164. Q. Zhu, Q. Huang, Y. Tian, S. Zhao, Y. Chen, G. Cao, K. Song, Y. Zhou, W. Yang, Z. Zhang, X. An, H. Zhou and J. Wang, *Sci. Adv.*, 2022, **8**, 8299.
165. X. Wang, J. Wang, Y. He, C. Wang, L. Zhong and S. X. Mao, *Nat. Commun.*, 2020, **11**, 2497.
166. B. Jiang, A. Tu, H. Wang, H. Duan, S. He, H. Ye and K. Du, *Acta Mater.*, 2018, **155**, 56-68.
167. J. A. Hawreliak, B. El-Dasher, H. Lorenzana, G. Kimminau, A. Higginbotham, B. Nagler, S. M. Vinko, W. J. Murphy, T. Whitcher, J. S. Wark, S. Rothman and N. Park, *Phys. Rev. B*, 2011, **83**.
168. Y. Bu, Y. Wu, Z. Lei, X. Yuan, L. Liu, P. Wang, X. Liu, H. Wu, J. Liu, H. Wang, R. O. Ritchie, Z. Lu and W. Yang, *Nat Commun*, 2024, **15**, 4599.
169. X. Li, Q. Wang, J. Fan, Y. Wang, Z. Zhang and J. Wang, *Mater. Sci. Eng., A*, 2022, **846**, 143274.
170. J. Song and W. A. Curtin, *Nat. Mater.*, 2013, **12**, 145-151.
171. J. Mei, Y. Ni and J. Li, *Int. J. Solids Struct.*, 2011, **48**, 3054-3062.
172. Y. Guo and D. Zhao, *Mater. Sci. Eng., A*, 2007, **448**, 281-286.
173. X. Li, W. Hu, S. Xiao and W.-Q. Huang, *Physica E*, 2011, **43**, 1131-1139.
174. W. Luo, D. Roundy, M. L. Cohen and J. W. Morris, *Phys. Rev. B*, 2002, **66**, 094110.
175. W. Yang, H. Sha, J. Cui, L. Mao and R. Yu, *Nat. Nanotechnol.*, 2024, **19**, 612-617.
176. J. J. P. Peters, B. W. Reed, Y. Jimbo, K. Noguchi, K. H. Muller, A. Porter, D. J. Masiel and L. Jones, *Science*, 2024, **385**, 549-553.
177. *Nat. Nanotechnol.*, 2020, **15**, 417.
178. E. A. Stach, D. Zakharov, R. D. Rivas, P. Longo, M. Lent, A. Gubbens and C. Czarnik, *Microsc. Microanal.*, 2013, **19**, 392-393.
179. A. Feist, N. Bach, N. Rubiano da Silva, T. Danz, M. Moller, K. E. Priebe, T. Domrose, J. G. Gatzmann, S. Rost, J. Schauss, S. Strauch, R. Bormann, M. Sivis, S. Schafer and C. Ropers, *Ultramicroscopy*, 2017, **176**, 63-73.
180. S. V. Kalinin, D. Mukherjee, K. Roccapriore, B. J. Blaiszik, A. Ghosh, M. A. Ziatdinov, A. Al-Najjar, C. Doty, S. Akers, N. S. Rao, J. C. Agar and S. R. Spurgeon, *npj Comput. Mater.*, 2023, **9**.
181. T. Fujita, P. Guan, K. McKenna, X. Lang, A. Hirata, L. Zhang, T. Tokunaga, S. Arai, Y. Yamamoto, N. Tanaka, Y. Ishikawa, N. Asao, Y. Yamamoto, J. Erlebacher and M. Chen, *Nat. Mater.*, 2012, **11**, 775-780.
182. Y. Yang, A. Kushima, W. Han, H. Xin and J. Li, *Nano Lett.*, 2018, **18**, 2492-2497.
183. D. Garcia, A. Leon and S. Kumar, *JOM*, 2015, **68**, 109-115.
184. X. Li, Y. Liu, Y. Zhao, Y. Chen, A. Li, J. Zhang, Y. Zhai, Z. Li, D. Ma, X. Li, Q. Zhang, X. Yang, H. Long, S. Mao, Z. Zhang and X. Han, *Mater. Res. Lett.*, 2021, **9**, 531-539.
185. S. Dai, Y. Hou, M. Onoue, S. Zhang, W. Gao, X. Yan, G. W. Graham, R. Wu and X. Pan, *Nano Lett.*, 2017, **17**, 4683-4688.
186. D. G. Xie, Z. J. Wang, J. Sun, J. Li, E. Ma and Z. W. Shan, *Nat. Mater.*, 2015, **14**, 899-903.
187. Y. Wang, B. Liu, X. Zhao, X. Zhang, Y. Miao, N. Yang, B. Yang, L. Zhang, W. Kuang, J. Li, E. Ma and Z. Shan, *Nat. Commun.*, 2018, **9**, 4058.
188. M. Li, D. G. Xie, E. Ma, J. Li, X. X. Zhang and Z. W. Shan, *Nat. Commun.*, 2017, **8**, 14564.
189. L. Huang, D. Chen, D. Xie, S. Li, Y. Zhang, T. Zhu, D. Raabe, E. Ma, J. Li and Z. Shan, *Nat.*

Mater., 2023, **22**, 710-716.
190. X. Wang, L. Zhong and S. X. Mao, *Mater. Today Nano*, 2018, **2**, 58-69.
191. R. G. Spruit, J. T. van Omme, M. K. Ghatkesar and H. H. P. Garza, *J. Microelectromech. Syst.*, 2017, **26**, 1165-1182.
192. J. Ma, J. Lu, L. Tang, J. Wang, L. Sang, Y. Zhang and Z. Zhang, *Rev. Sci. Instrum.*, 2020, **91**, 043704.
193. K. Srivastava, D. Weygand, D. Caillard and P. Gumbsch, *Nat. Commun.*, 2020, **11**, 5098.
194. Y. Deng, C. Gammer, J. Ciston, P. Ercius, C. Ophus, K. Bustillo, C. Song, R. Zhang, D. Wu, Y. Du, Z. Chen, H. Dong, A. G. Khachaturyan and A. M. Minor, *Acta Mater.*, 2019, **181**, 501-509.
195. Y. Yang, J. Zhou, F. Zhu, Y. Yuan, D. J. Chang, D. S. Kim, M. Pham, A. Rana, X. Tian, Y. Yao, S. J. Osher, A. K. Schmid, L. Hu, P. Ercius and J. Miao, *Nature*, 2021, **592**, 60.
196. D. A. Muller, *Nat. Mater.*, 2009, **8**, 263-270.
197. M. Song, G. Zhou, N. Lu, J. Lee, E. Nakouzi, H. Wang and D. Li, *Science*, 2020, **367**, 40-45.
198. Z. J. Wang, Q. J. Li, Y. Li, L. C. Huang, L. Lu, M. Dao, J. Li, E. Ma, S. Suresh and Z. W. Shan, *Nat. Commun.*, 2017, **8**, 1108.
199. Y. Chen, S. Zhao, Q. Huang, Q. Zhu, K. Song, H. Zhou and J. Wang, *Int. J. Plast.*, 2022, **148**, 103128.
200. Q. Zhu, G. Cao, J. Wang, C. Deng, J. Li, Z. Zhang and S. X. Mao, *Nat. Commun.*, 2019, **10**, 156.
201. Q. Zhu, S. C. Zhao, C. Deng, X. H. An, K. X. Song, S. X. Mao and J. W. Wang, *Acta Mater.*, 2020, **199**, 42-52.
202. C. Wang, H. Duan, C. Chen, P. Wu, D. Qi, H. Ye, H.-J. Jin, H. L. Xin and K. Du, *Matter*, 2020, **3**, 1999-2011.
203. Q. He, S. Schmidt, W. Zhu, G. Wu, T. Huang, L. Zhang, D. J. Jensen, Z. Feng, A. Godfrey and X. Huang, *Science*, 2023, **382**, 1065-1069.
204. L. G. Sun, G. Wu, Q. Wang and J. Lu, *Mater. Today*, 2020, **38**, 114-135.
205. Z. Zhang, H. Sheng, Z. Wang, B. Gludovatz, Z. Zhang, E. P. George, Q. Yu, S. X. Mao and R. O. Ritchie, *Nat. Commun.*, 2017, **8**, 14390.
206. Q. Zhang, R. Niu, Y. Liu, J. Jiang, F. Xu, X. Zhang, J. M. Cairney, X. An, X. Liao, H. Gao and X. Li, *Nat. Commun.*, 2023, **14**, 7469.
207. C. Yang, B. Zhang, L. Fu, Z. Wang, J. Teng, R. Shao, Z. Wu, X. Chang, J. Ding, L. Wang and X. Han, *Nat. Commun.*, 2023, **14**, 5705.
208. F. Wang, M. Song, M. Elkot, N. Yao, B. Sun, M. Song, Z. Wang and D. Raabe, *Science*, 2024, **384**, 1017-1022.
209. Y. Yue, Y. Gao, W. Hu, B. Xu, J. Wang, X. Zhang, Q. Zhang, Y. Wang, B. Ge, Z. Yang, Z. Li, P. Ying, X. Liu, D. Yu, B. Wei, Z. Wang, X.-F. Zhou, L. Guo and Y. Tian, *Nature*, 2020, **582**, 370-374.
210. Y. Hong, H. Wang, X. Li, L. Zhong, H. Chen, Z. Zhang, P. Cao, R. O. Ritchie and J. Wang, *Matter*, 2023, **6**, 1160-1172.
211. B. Wu, A. Heidelberg and J. J. Boland, *Nat. Mater.*, 2005, **4**, 525-529.
212. J. Uzuhashi and T. Ohkubo, *Ultramicroscopy*, 2024, **262**, 113980.
213. Y. He, D. She, Z. Liu, X. Wang, L. Zhong, C. Wang, G. Wang and S. X. Mao, *Nat. Mater.*, 2021, **21**, 173-180.

214. X. Wang, Z. Liu, Y. He, S. Tan, G. Wang and S. X. Mao, *Nat. Nanotechnol.*, 2022, **17**, 737-745.
215. T. Sato, Z. B. Milne, M. Nomura, N. Sasaki, R. W. Carpick and H. Fujita, *Nat Commun*, 2022, **13**, 2551.

No primary research results, software or code have been included and no new data were generated or analysed as part of this review.